Unstable Interactions between a Hurricane's Primary Eyewall and a Secondary Ring of Enhanced Vorticity

JAMES P. KOSSIN, WAYNE H. SCHUBERT, AND MICHAEL T. MONTGOMERY

Department of Atmospheric Science, Colorado State University, Fort Collins, Colorado

(Manuscript received 17 August 1999, in final form 10 March 2000)

ABSTRACT

Intense tropical cyclones often exhibit concentric eyewall patterns in their radar reflectivity. Deep convection within the inner, or primary, eyewall is surrounded by a nearly echo-free moat, which in turn is surrounded by an outer, or secondary ring of deep convection. Both convective regions typically contain well-defined tangential wind maxima. The primary wind maximum is associated with large vorticity just inside the radius of maximum wind, while the secondary wind maximum is usually associated with relatively enhanced vorticity embedded in the outer ring. In contrast, the moat is a region of low vorticity. If the vorticity profile across the eye and inner eyewall is approximated as monotonic, the resulting radial profile of vorticity still satisfies the Rayleigh necessary condition for instability as the radial gradient twice changes sign.

Here the authors investigate the stability of such structures and, in the case of instability, simulate the nonlinear evolution into a more stable structure using a nondivergent barotropic model. Because the radial gradient of vorticity changes sign twice, two types of instability and vorticity rearrangement are identified: 1) instability across the outer ring of enhanced vorticity, and 2) instability across the moat. Type 1 instability occurs when the outer ring of enhanced vorticity is sufficiently narrow and when the circulation of the central vortex is sufficiently weak (compared to the outer ring) that it does not induce enough differential rotation across the outer ring to stabilize it. The nonlinear mixing associated with type 1 instability results in a broader and weaker vorticity ring but still maintains a significant secondary wind maximum. The central vortex induces strong differential rotation (and associated enstrophy cascade) in the moat region, which then acts as a barrier to inward mixing of small (but finite) amplitude asymmetric vorticity disturbances. Type 2 instability occurs when the radial extent of the moat is sufficiently narrow so that unstable interactions may occur between the central vortex and the inner edge of the ring. Because the vortex-induced differential rotation across the ring is large when the ring is close to the vortex, type 2 instability typically precludes type 1 instability except in the case of very thin rings. The nonlinear mixing from type 2 instability perturbs the vortex into a variety of shapes. In the case of contracting rings of enhanced vorticity, the vortex and moat typically evolve into a nearly steady tripole structure, thereby offering a mechanism for the formation and persistence of elliptical eyewalls.

1. Introduction

During the period 11–17 September 1988, Hurricane Gilbert moved westward across the Caribbean Sea, over the tip of the Yucatan peninsula, and across the Gulf of Mexico, making landfall just south of Brownsville, Texas. After passing directly over Jamaica on 12 September, Gilbert intensified rapidly and at 2152 UTC on 13 September reached a minimum sea level pressure of 888 mb, the lowest yet recorded in the Atlantic basin (Willoughby et al. 1989). Approximately 12 h later, when its central pressure was 892 mb, the horizontal structure of the radar reflectivity and the radial profiles of tangential wind, angular velocity, and relative vorticity were as shown in Fig. 1. At this time the storm had concentric eyewalls. The inner eyewall was between 8- and 20-km radius and the outer eyewall between 55- and 100-km radius, with a 35-km echo-free gap (or moat) between the inner and outer eyewalls. The inner tangential wind maximum was 66–69 m s^{-1} at 10-km radius, while the outer tangential wind maximum was 49–52 m s^{-1} at 61–67-km radius. Detailed descriptions of Hurricane Gilbert are given by Black and Willoughby (1992), Samsury and Zipser (1995), and Dodge et al. (1999).

Echo-free moats such as the one shown in Fig. 1 are often found in intense storms, even when no well-defined outer eyewall is present. In general, echo-free moats are regions of strong differential rotation.[1] For

Corresponding author address: James P. Kossin, Department of Atmospheric Science, Colorado State University, Fort Collins, CO 80523.
E-mail: kossin@euler.atmos.colostate.edu

[1] We define differential rotation as $d\overline{\omega}/dr$, where $\overline{\omega}$ is the azimuthal mean angular velocity.

© 2000 American Meteorological Society

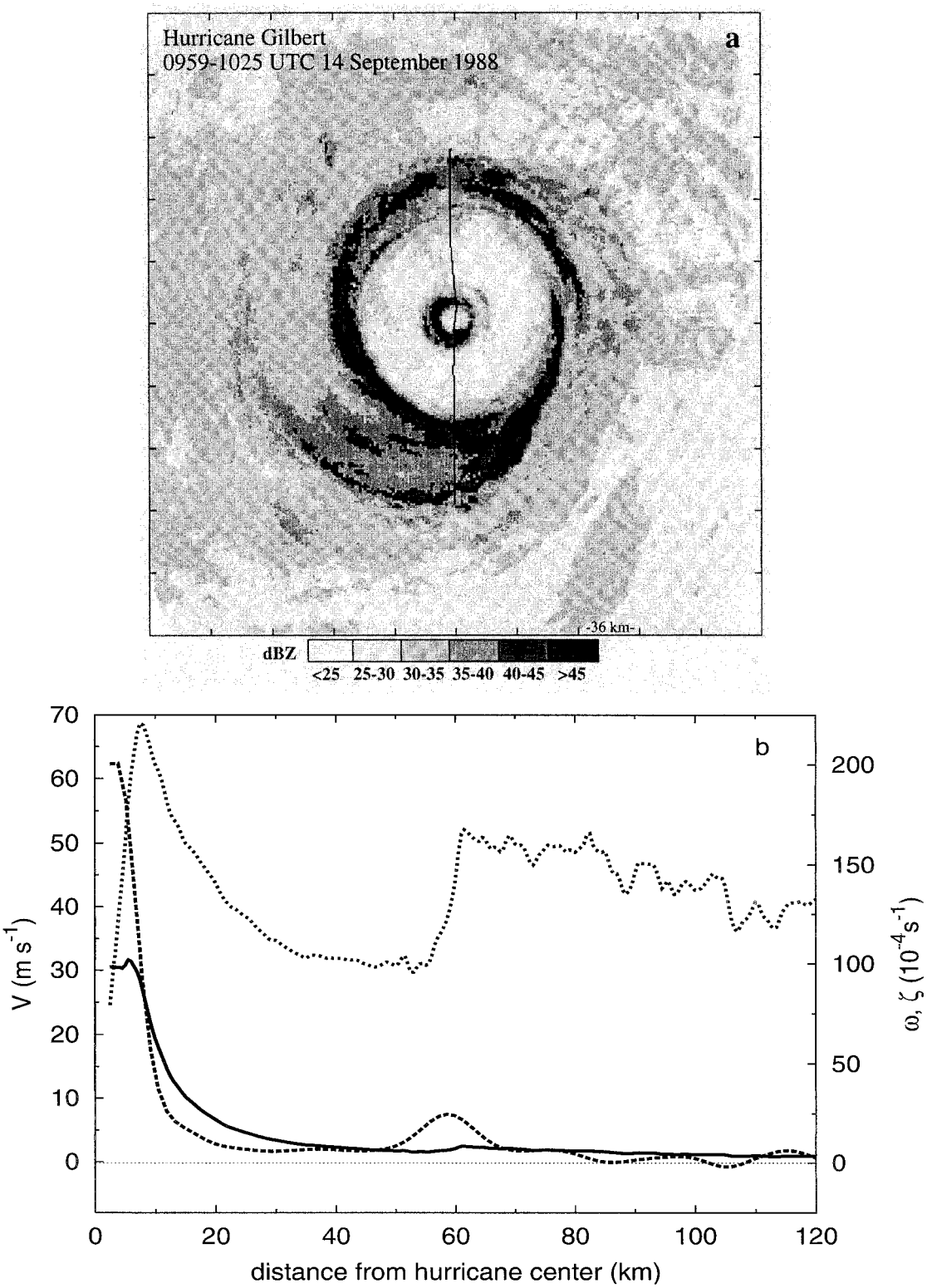

FIG. 1. (a) Composite horizontal radar reflectivity of Hurricane Gilbert for 0959–1025 UTC 14 Sep 1988; the domain is 360 km × 360 km, with tick marks every 36 km. The line through the center is the WP-3D aircraft flight track (from Samsury and Zipser 1995). (b) Profiles of flight-level angular velocity (solid), tangential wind (short dash), and smoothed relative vorticity (long dash) along the southern leg of the flight track shown in (a).

example, in the Gilbert case, the circuit time (i.e., the time required to traverse a complete circle) for a parcel at a radius of 10 km, with tangential wind 68 m s^{-1}, is 15.4 min, while the circuit time for a parcel at a radius of 50 km, with tangential wind 30 m s^{-1}, is 175 min. In other words, the parcel at 10-km radius completes 11 circuits in the time the parcel at 50-km radius completes one circuit. Under such strong differential rotation, small asymmetric regions of enhanced potential vorticity are rapidly filamented to small radial scales (Carr and Williams 1989; Sutyrin 1989; Smith and Montgomery 1995) as they become more axisymmetric. Thus, the moat is typically a region of active potential enstrophy cascade to small scales. In contrast, the region just inside the secondary wind maximum has weak differential rotation. For example, the circuit time for a parcel at 61-km radius, with tangential wind 52 m s^{-1}, is 123 min, compared to the previously computed 175 min at 50-km radius. Hence, the region between 50 and 61 km is characterized by weak differential rotation and can be considered a local haven against the ravages of potential enstrophy cascade to small scales. Similarly, the updraft cores within the primary eyewall are typically embedded in the local minimum of differential rotation that lies just inside the radius of maximum wind. This is evident in Fig. 1b, which shows a flattening of the angular velocity profile inside the wind maximum.

The tendency for convection to be suppressed in the moat region is often attributed to mesoscale subsidence between two regions of strong upward motion. Dodge et al. (1999) found that the moat of Hurricane Gilbert consisted of stratiform precipitation with weak (less than 1 m s^{-1}) downward motion below the bright band observed near 5-km height, and weak upward motion above. An additional mechanism for suppressed convection in the moat may be strong differential rotation. For example, imagine a circular 5-km-diameter cloud updraft that lies between 15- and 20-km radius from the hurricane center. For the Gilbert wind field, the inner edge of this updraft would be advected azimuthally 140° in 10 min, while the outer edge is advected 70° in 10 min. Since a parcel rising at 5 m s^{-1} ascends only 3 km in this 10-min interval, one could imagine that ordinary cumulonimbus convection embedded in such a flow would be inhibited from persisting as the convection becomes increasingly susceptible to entrainment.

Concentric eyewall structures and tangential wind profiles like those shown in Fig. 1 have been documented in a number of hurricanes (Samsury and Zipser 1995; Willoughby et al. 1982, and references therein) and raise interesting questions about the dynamic stability of hurricane flows. The answers to such questions require studies using a hierarchy of dynamical models, the simplest of which is the nondivergent barotropic model. In such a model, Hurricane Gilbert, for example, might be idealized as an axisymmetric flow field with four distinct regions of vorticity: an inner region ($r < r_1 \approx 10$ km) of very high vorticity $\zeta_1 \approx 159 \times 10^{-4}$ s^{-1}, a moat region ($r_1 < r < r_2 \approx 55$ km) of relatively low vorticity $\zeta_2 \approx 5 \times 10^{-4}$ s^{-1}, an annular ring ($r_2 < r < r_3 \approx 100$ km) of elevated vorticity $\zeta_3 \approx 27 \times 10^{-4}$ s^{-1}, and the far field ($r > r_3$) nearly irrotational flow. The assumption of a monotonic profile near the vortex center removes the possibility for primary eyewall instabilities, which were the focus of Schubert et al. (1999). In this idealization, vorticity gradients and associated vortex Rossby waves are concentrated at the radii r_1, r_2, r_3. In this case, there are two types of instabilities, as the vortex Rossby wave on the positive radial vorticity gradient at r_2 can interact with either of the vortex Rossby waves on the negative radial vorticity gradients at r_1 and r_3.

In the first type of instability (called type 1), the dominant interactions occur between the waves associated with r_2 and r_3. The central vorticity does not play a direct role in this instability, because the vorticity wave at r_1 is dynamically inactive. However, the central vorticity does induce a differential rotation between r_2 and r_3, and this differential rotation can help suppress the instability across the ring of elevated vorticity between r_2 and r_3 (Dritschel 1989). Type 1 instability leads to a roll-up of the annular ring and the formation of coherent vorticity structures. Once roll-up has occured, the flow evolution is described by a collection of vortex merger events in which the central vortex is victorious (Melander et al. 1987b; Dritschel and Waugh 1992) in the sense that the vorticity within the central vortex remains largely unchanged while the relatively weak coherent vortices become rapidly filamented and axisymmetrized by the differential rotation imposed across the moat by the intense central vortex. The result is a widening of the annular ring of elevated vorticity and a weakening but ultimate maintenance of the secondary wind maximum. This type of evolution is discussed in section 2.

In the second type of instability (called type 2), the dominant interactions occur between the waves associated with r_1 and r_2, that is, across the moat. In this case, type 1 instabilities are largely or completely suppressed by the presence of the central vortex. Type 2 instability leads to a rearrangement of the low vorticity of the moat. One possible nonlinear outcome of this instability is the production of a vortex tripole in which the low vorticity of the moat pools into two satellites of an elliptically deformed central vortex, with the whole structure rotating cyclonically. This type of evolution is discussed in section 3.

2. Stabilization of an annular ring of vorticity by a strong central vortex

a. Linear stability analysis

The cyclonic shear zone associated with a secondary eyewall can be envisaged as an annular ring of uni-

formly high vorticity, with large radial vorticity gradients on its edges. On the inner edge of the annular ring the vorticity increases with radius, while on the outer edge the vorticity decreases with radius. In terms of vortex Rossby wave theory, waves on the inner edge of the annular ring will prograde relative to the flow there, while waves on the outer edge will retrograde relative to the flow there. It is possible for these two counterpropagating (relative to the tangential flow in their vicinity) waves to have the same angular velocity relative to the earth, that is, to be phase locked. If the locked phase is favorable, each wave will make the other grow, and barotropic instability will result. The presence of a central region of high vorticity complicates this picture in two ways. First, the edge of the central region can also support waves, which might interact with waves along the other two edges if they are close enough (section 3). Second, even if the annular ring of elevated vorticity between r_2 and r_3 is far enough away from the central region that the waves along the edge of the central region do not significantly interact, the central region of high vorticity can induce an axisymmetric differential rotation across the annular ring and thereby stabilize the ring. Both of these effects can be understood as special cases of a four-region model, which is discussed in the appendix. The main result of that analysis is the eigenvalue problem (A6). In order to understand the stabilizing effect of differential rotation across the annular ring, we first consider the special case where $\zeta_2 = 0$, and where $r_1 \to 0$ and $\zeta_1 \to \infty$ in such a way that $\pi r_1^2 \zeta_1 = 2\pi r_1^2 \overline{\omega}_1 \to C$, where C is a specified constant circulation associated with the central point vortex. In this special case the axisymmetric basic state angular velocity $\overline{\omega}(r)$ given by (A2) reduces to

$$\overline{\omega}(r) = \frac{C}{2\pi r^2} + \frac{1}{2}\zeta_3 \begin{cases} 0 & 0 \le r \le r_2, \\ 1 - (r_2/r)^2 & r_2 \le r \le r_3, \\ (r_3/r)^2 - (r_2/r)^2 & r_3 \le r < \infty, \end{cases} \tag{1}$$

and the corresponding basic state relative vorticity $\overline{\zeta}(r)$ given by (A3) reduces to

$$\overline{\zeta}(r) = \frac{d(r^2\overline{\omega})}{rdr} = \begin{cases} 0 & 0 < r < r_2, \\ \zeta_3 & r_2 < r < r_3, \\ 0 & r_3 < r < \infty, \end{cases} \tag{2}$$

where r_2, r_3 are specified radii and ζ_3 a specified vorticity level. This idealized basic state was also studied by Dritschel (1989). The eigenvalue problem (A6) reduces to

$$\begin{bmatrix} m\overline{\omega}_2 + \frac{1}{2}\zeta_3 & \frac{1}{2}\zeta_3(r_2/r_3)^m \\ -\frac{1}{2}\zeta_3(r_2/r_3)^m & m\overline{\omega}_3 - \frac{1}{2}\zeta_3 \end{bmatrix} \begin{pmatrix} \Psi_2 \\ \Psi_3 \end{pmatrix} = \nu \begin{pmatrix} \Psi_2 \\ \Psi_3 \end{pmatrix}. \tag{3}$$

The system (3) can be regarded as a concise mathematical description of the interaction between two counterpropagating vortex Rossby edge waves along r_2 and r_3 and influenced by the central vortex. As we shall see below, with a basic flow satisfying $\overline{\omega}_2 < \overline{\omega}_3$, the waves can phase lock, and instability is possible. Note that the effects of the central point vortex enter through $\overline{\omega}_2$ and $\overline{\omega}_3$. The effect of a strong central vortex is to make $\overline{\omega}_2 > \overline{\omega}_3$, which disrupts the ability of the two waves to phase lock. To quantify the effects of the central point vortex on the stability of the annular ring, let us now examine the formula for the eigenvalues ν.

The eigenvalues of (3), normalized by ζ_3, are given by

$$\frac{\nu}{\zeta_3} = \frac{1}{2}m\left(\frac{\overline{\omega}_2 + \overline{\omega}_3}{\zeta_3}\right) \pm \frac{1}{2}\left\{\left[1 + m\left(\frac{\overline{\omega}_2 - \overline{\omega}_3}{\zeta_3}\right)\right]^2 - \left(\frac{r_2}{r_3}\right)^{2m}\right\}^{1/2}. \tag{4}$$

In order to more easily interpret the eigenvalue relation (4), it is convenient to reduce the number of adjustable parameters to two. We first define $\delta = r_2/r_3$ as a measure of the width of the annular ring of vorticity and $\Gamma = C/[\pi\zeta_3(r_3^2 - r_2^2)]$ as the ratio of the central point vortex circulation to the secondary eyewall circulation. Expressing $\overline{\omega}_2/\zeta_3$ and $\overline{\omega}_3/\zeta_3$ in terms of Γ and δ, it can be shown using (4) that wavenumbers one and two are exponentially stable when $\Gamma > 0$, and for $m > 2$, stability is guaranteed when

$$\Gamma > \frac{\delta^2}{1 - \delta^2}. \tag{5}$$

The stability condition (5) is equivalent to Dritschel's (1989) condition, $\Lambda > 1$, where $\Lambda = C/(\pi\zeta_3 r_2^2)$ is a dimensionless "adverse shear." The region of the Γ–δ plane satisfying (5) lies above the dashed lines in Figs. 2 and 3. A physical interpretation of the stability condition (5) is related to Fjørtoft's theorem (Montgomery and Shapiro 1995) and can be understood by noting that since the right-hand side of (5) is less than unity and the left-hand side is greater than unity if $(\overline{\omega}_2 - \overline{\omega}_3)/\zeta_3 > 0$, stability is assured if $\overline{\omega}_2 > \overline{\omega}_3$ (for $\zeta_3 > 0$). Since, in the absence of coupling, the waves on the inner edge of the annular ring prograde relative to the flow in its vicinity, and since the waves on the outer edge retrograde relative to the flow in its vicinity, a larger basic-state angular velocity on the inner edge ($\overline{\omega}_2 > \overline{\omega}_3$) will prevent the waves from phase locking, satisfying a sufficient condition for stability.

Wavenumbers larger than two can produce frequencies with nonzero imaginary parts. Expressing $\overline{\omega}_2/\zeta_3$ and $\overline{\omega}_3/\zeta_3$ in terms of δ and Γ as $\overline{\omega}_2/\zeta_3 = \frac{1}{2}\Gamma(\delta^{-2} - 1)$ and $\overline{\omega}_3/\zeta_3 = \frac{1}{2}(\Gamma + 1)(1 - \delta^2)$, and then using these in (4), we can calculate the dimensionless complex frequency ν/ζ_3 as a function of the disturbance azimuthal wavenumber m and the two basic-state flow parameters δ and Γ. The imaginary part of ν/ζ_3, de-

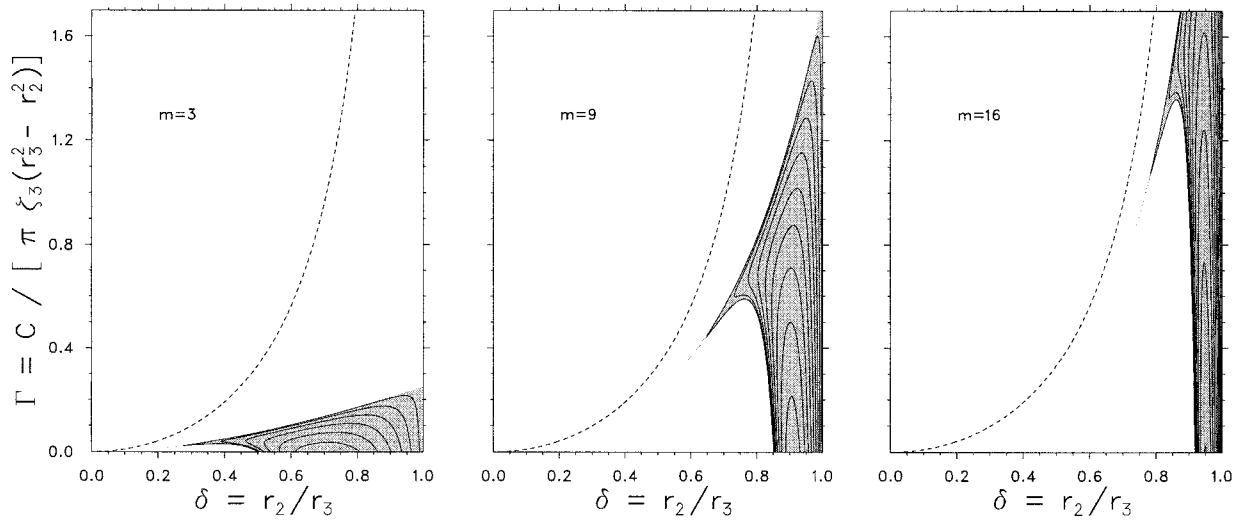

FIG. 2. Isolines of the dimensionless growth rate ν_i/ζ_3, computed from (4), as a function of $\delta = r_2/r_3$ and $\Gamma = C/[\pi\zeta_3(r_3^2 - r_2^2)]$ for azimuthal wavenumbers $m = 3$, 9, and 16. The parameter Γ is the ratio of the circulation associated with the central point vortex to the circulation associated with the annular ring of elevated vorticity between r_2 and r_3. Nonzero growth rates occur only in the shaded regions. The isolines are $\nu_i/\zeta_3 = 0.01, 0.03, 0.05, \ldots$. The maximum growth rates increase and are found closer to $\delta = 1$ as m increases. The region above the dashed line satisfies the sufficient condition for stability given by (5).

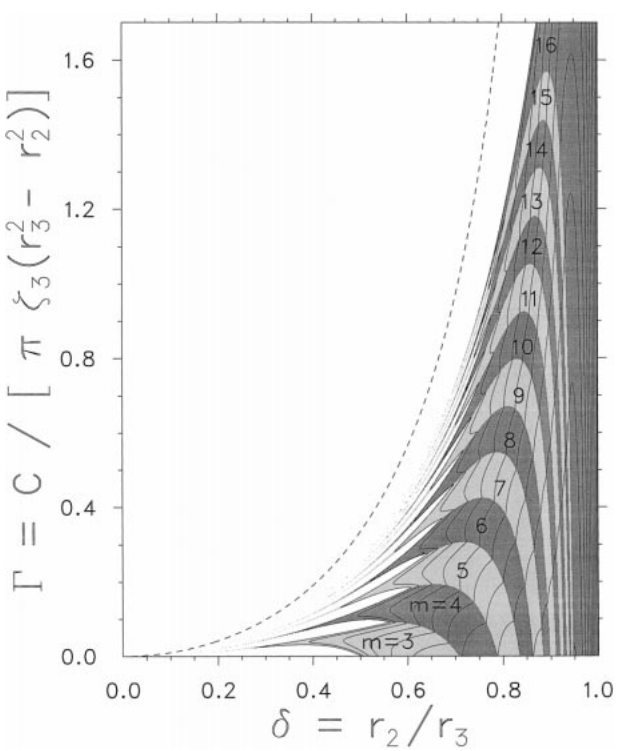

FIG. 3. Isolines of the maximum dimensionless growth rate ν_i/ζ_3 among the azimuthal wavenumbers $m = 3, 4, \ldots, 16$ for type 1 instability. The isolines are the same as in Fig. 2. Shading indicates the wavenumber associated with the maximum dimensionless growth rate at each point.

noted by ν_i/ζ_3, is a dimensionless measure of the growth rate. Isolines of ν_i/ζ_3 as a function of δ and Γ for $m = 3$, 9, and 16 are shown in Fig. 2. Note that all basic states, no matter what the value of Γ, satisfy the Rayleigh necessary condition for instability, but that most of the region shown in Fig. 2 is in fact stable. Clearly, thinner annular regions (larger values of r_2/r_3) should produce the highest growth rates but at much higher azimuthal wavenumbers. Note also the overlap in the unstable regions of the Γ–δ plane for different azimuthal wavenumbers. For example, the lower right area of the Γ–δ plane is unstable to all the azimuthal wavenumbers $m = 3$, 9, and 16. We can combine the three panels in Fig. 2 with the remaining growth rate plots for $m = 3, 4, \ldots, 16$ and collapse them into a single diagram if, for each point in the Γ–δ plane, we choose the largest growth rate of the fourteen wavenumbers. This results in Fig. 3.

To estimate the growth rates expected in a secondary eyewall mixing problem, consider the cases $\delta \approx 0.84$ and $\Gamma \approx 0.45$, which are suggested by the Hurricane Gilbert data shown in Fig. 1 (but for the special case of $\zeta_2 = 0$). Then, from the isolines drawn in Fig. 3, we obtain $\nu_i \approx 0.12\zeta_3$ for $m = 8$. Using $\zeta_3 \approx 2.8 \times 10^{-3}$ s^{-1}, we obtain an e-folding time $\nu_i^{-1} \approx 50$ min. The analysis of section 2c, where the restriction that $\zeta_2 = 0$ is relaxed, results in a maximum instability for $m = 9$.

b. Nondivergent barotropic spectral model

To isolate the barotropic aspects of the nonlinear evolution, we now consider the nondivergent barotropic

model with spectral discretization and ordinary diffusion. Expressing the velocity components[2] in terms of the streamfunction by $u = -\partial\psi/\partial y$ and $v = \partial\psi/\partial x$, we can write the vorticity equation as

$$\frac{\partial\zeta}{\partial t} + \frac{\partial(\psi, \zeta)}{\partial(x, y)} = \nu\nabla^2\zeta, \tag{6}$$

where

$$\nabla^2\psi = \zeta \tag{7}$$

is the invertibility principle. Two integral properties associated with (6) and (7) on a closed or periodic domain are the energy and enstrophy relations

$$\frac{d\mathcal{E}}{dt} = -2\nu\mathcal{Z}, \tag{8}$$

$$\frac{d\mathcal{Z}}{dt} = -2\nu\mathcal{P}, \tag{9}$$

where $\mathcal{E} = \iint \frac{1}{2}\nabla\psi \cdot \nabla\psi \, dx \, dy$ is the energy, $\mathcal{Z} = \iint \frac{1}{2}\zeta^2 \, dx \, dy$ is the enstrophy, and $\mathcal{P} = \iint \frac{1}{2}\nabla\zeta \cdot \nabla\zeta \, dx \, dy$ is the palinstrophy. The diffusion term on the right-hand side of (6) controls the spectral blocking associated with the enstrophy cascade to higher wavenumbers.

We now present numerical integrations of (6)–(7) that demonstrate the process by which an unstable outer ring of enhanced vorticity mixes with its near environment to form a broader and weaker vorticity ring. All of the solutions presented in this paper were obtained with a double Fourier pseudospectral code having 1024×1024 equally spaced collocation points on a doubly periodic domain of size 600 km $\times$ 600 km. The code was run with a dealiased calculation of the quadratic nonlinear terms in (6), resulting in 340 $\times$ 340 resolved Fourier modes. Although the collocation points are only 0.585 km apart, a more realistic estimate of resolution is the wavelength of the highest Fourier mode, which is 1.76 km. Time differencing was accomplished with a standard fourth-order Runge–Kutta scheme. For the experiment of section 2c, the time step used was 7.5 s and the chosen value of viscosity in (6) was $\nu = 4 \text{ m}^2 \text{ s}^{-1}$, resulting in a $1/e$ damping time of 5.5 h for all modes having total wavenumber 340. However, for modes having total wavenumber 170, the damping time lengthens considerably to 22 h. For the experiment of section 2d, the time step used was 15 s and the chosen value of viscosity was $\nu = 32 \text{ m}^2 \text{ s}^{-1}$. This gives $1/e$ damping times of 41 min and 3 h for all modes having total wavenumber 340 and 170, respectively. The larger value of viscosity used in the second experiment was chosen in response to the more vigorous mixing and associated palinstrophy production and enstrophy cascade that occurs during the integration.

As the initial condition for (6), we use $\zeta(r, \phi, 0) = \overline{\zeta}(r) + \zeta'(r, \phi)$ where

$$\overline{\zeta}(r) = \begin{cases} \zeta_1, & 0 \le r \le r_1 - d_1 \\ \zeta_1 S[(r - r_1 + d_1)/2d_1] + \zeta_2 S[(r_1 + d_1 - r)/2d_1], & r_1 - d_1 \le r \le r_1 + d_1 \\ \zeta_2, & r_1 + d_1 \le r \le r_2 - d_2 \\ \zeta_2 S[(r - r_2 + d_2)/2d_2] + \zeta_3 S[(r_2 + d_2 - r)/2d_2], & r_2 - d_2 \le r \le r_2 + d_2 \\ \zeta_3, & r_2 + d_2 \le r \le r_3 - d_3 \\ \zeta_3 S[(r - r_3 + d_3)/2d_3] + \zeta_4 S[(r_3 + d_3 - r)/2d_3], & r_3 - d_3 \le r \le r_3 + d_3 \\ \zeta_4, & r_3 + d_3 \le r \le r_4 - d_4 \\ \zeta_4 S[(r - r_4 + d_4)/2d_4] + \zeta_5 S[(r_4 + d_4 - r)/2d_4], & r_4 - d_4 \le r \le r_4 + d_4 \\ \zeta_5, & r_4 + d_4 \le r \end{cases} \tag{11}$$

is a circular four-region vorticity distribution and r_1, r_2, r_3, r_4, d_1, d_2, d_3, d_4, ζ_1, ζ_2, ζ_3, ζ_4 are independently specified quantities. The constant ζ_5 will be determined in order to make the domain average of $\zeta(r, \phi, 0)$ vanish. Here $S(s) = 1 - 3s^2 + 2s^3$ is the basic cubic Hermite shape function satisfying $S(0) = 1$, $S(1) = 0$, $S'(0) = S'(1) = 0$. Since ζ_5 must generally be weakly negative to satisfy the zero circulation requirement, but no negative vorticity is expected in the region of hurricanes, we apply a small but positive "far field" vorticity ζ_4 to a radius beyond the area of expected mixing processes. For the experiments of sections 2c and 2d, we apply an azimuthally broadband perturbation across the annular region $r_2 - d_2 \le r \le r_3 + d_3$, that is,

[2] Throughout this paper the symbols u, v are used to denote eastward and northward components of velocity when working in Cartesian coordinates and to denote radial and tangential components when working in cylindrical coordinates.

$$\zeta'(r, \phi) = \zeta_{\text{amp}} \sum_{m=1}^{12} \cos(m\phi) \begin{cases} 0, & 0 \le r \le r_2 - d_2 \\ S[(r_2 + d_2 - r)/2d_2], & r_2 - d_2 \le r \le r_2 + d_2 \\ 1, & r_2 + d_2 \le r \le r_3 - d_3 \\ S[(r - r_3 + d_3)/2d_3], & r_3 - d_3 \le r \le r_3 + d_3 \\ 0, & r_3 + d_3 \le r < \infty \end{cases} \tag{12}$$

where ζ_{amp} is a specified constant less than 1% of the maximum vorticity in the annulus.

c. *Type 1 instability in the presence of a central vortex: Maintenance of a secondary wind maximum*

An initial condition that simulates an annular ring of high potential vorticity (PV) with concentrated vorticity at its center may be imposed by choosing $\zeta_1 \gg \zeta_3 > \zeta_2$ and $r_1 \ll r_2$ in (11). In this way, wave interactions between the ring and the central vortex are minimized and the ring ''feels'' the presence of the central vortex only through the angular velocity field. For the first experiment, the numerical integration is performed under the initial condition $\{r_1, r_2, r_3, r_4\} = \{9.5, 52.5, 62.5, 120.0\}$ km, $\{d_1, d_2, d_3, d_4\} = \{2.5, 2.5, 2.5, 15.0\}$ km, and $\{\zeta_1, \zeta_2, \zeta_3, \zeta_4, \zeta_5\} = \{159.18, 5.18, 27.18, 2.18, -0.82\} \times 10^{-4}$ s^{-1}. The associated tangential wind profile is analogous to an observed profile from a single National Oceanic and Atmospheric Administration (NOAA) WP-3D radial flight leg into Hurricane Gilbert during 1012–1029 UTC 14 September 1988 (as shown in Fig. 1). Radial profiles of the symmetric part of the initial vorticity, tangential wind, and angular velocity fields are shown by the solid lines in Fig. 4 (the other lines in this figure will be discussed later). The maximum wind of 69 m s^{-1} is found near 10 km, while a secondary maximum of 47 m s^{-1}, associated with the ring of enhanced vorticity, is evident near 64 km. The prograding vortex Rossby waves along the inner edge of the ring ($50 \le r \le 55$ km) are embedded in a local angular velocity of approximately 5.6×10^{-4} s^{-1}, while the retrograding waves along the outer edge of the ring ($60 \le r \le 65$ km) are embedded in a stronger local angular velocity of approximately 7.3×10^{-4} s^{-1}. Although the presence of the central vortex reduces the differential rotation across the annular ring by about 30% when compared to the differential rotation with the central vortex removed, it is not enough to eliminate all instabilities. A piecewise uniform vorticity profile as described in the four-region model of the appendix and that imitates the smooth initial vorticity profile of Fig. 4 is found to be unstable in wavenumbers seven through 10, with the maximum growth rate occuring in wavenumber nine with an associated *e*-folding time of 67 minutes (solid line of Fig. 5).

Results of this experiment are shown in Fig. 6 in the form of vorticity maps plotted over a 24-h period. The growth of the wavenumber-nine maximum instability becomes evident within 4 h and by $t = 6$ h the ring has undergone a nearly complete roll-up into nine coherent structures. The differential rotation induced by the central vortex advects the inner edges of the coherent structures more rapidly than the outer edges so that at $t = 8$ h, the structures have become cyclonically stretched around the vortex, while trailing spirals have formed as vorticity is stripped from their outer edges. At $t = 10$ h, the stretching has resulted in a banded structure with thin strips of enhanced vorticity being wrapped around the vortex. Leading spirals, which have been stripped from the inner edges of the bands, have propagated inward into regions of intense differential rotation (and active enstrophy cascade). At $t = 12$ h, the moat has been maintained, although its outer radius has contracted to 35 km from its initial value of 60 km. Outside $r = 35$ km, the vorticity of the strips is sufficiently strong to maintain the strips against the vortex-induced differential rotation. Inside $r = 35$ km, the strips can no longer maintain themselves and they are rapidly filamented to small scales where they are lost to diffusion. Thus for these initial conditions, $r = 35$ km represents a barrier to inward mixing. Also evident at this time, particularly in the two eastern quadrants of the vortex, are secondary instabilities across individual strips of vorticity. These instabilities occur as the strips become thinner and are most pronounced at larger radii where the vortex-induced differential rotation is weak. The occurence of secondary instabilities in our experiment can be related to the results of Dritschel (1989) by estimating the adverse shear $\Lambda = C/(\pi\zeta_3 r_2^2)$ across these strips. Using $C \approx \pi\zeta_1 r_1^2$, we obtain $\Lambda \approx 0.187$. For the case of a linear shear flow, Dritschel found that such secondary instabilities lead to a roll-up into a string of vortices when $\Lambda < 0.21$, while for larger Λ, the adverse shear inhibits this secondary roll-up even though the strips are in fact unstable. We see then that the presence of a central vortex influences the flow evolution in two somewhat disparate ways. In the region of the moat, coherent vorticity structures are filamented and lost to diffusion, while at larger radii (but still inside $r = 80$

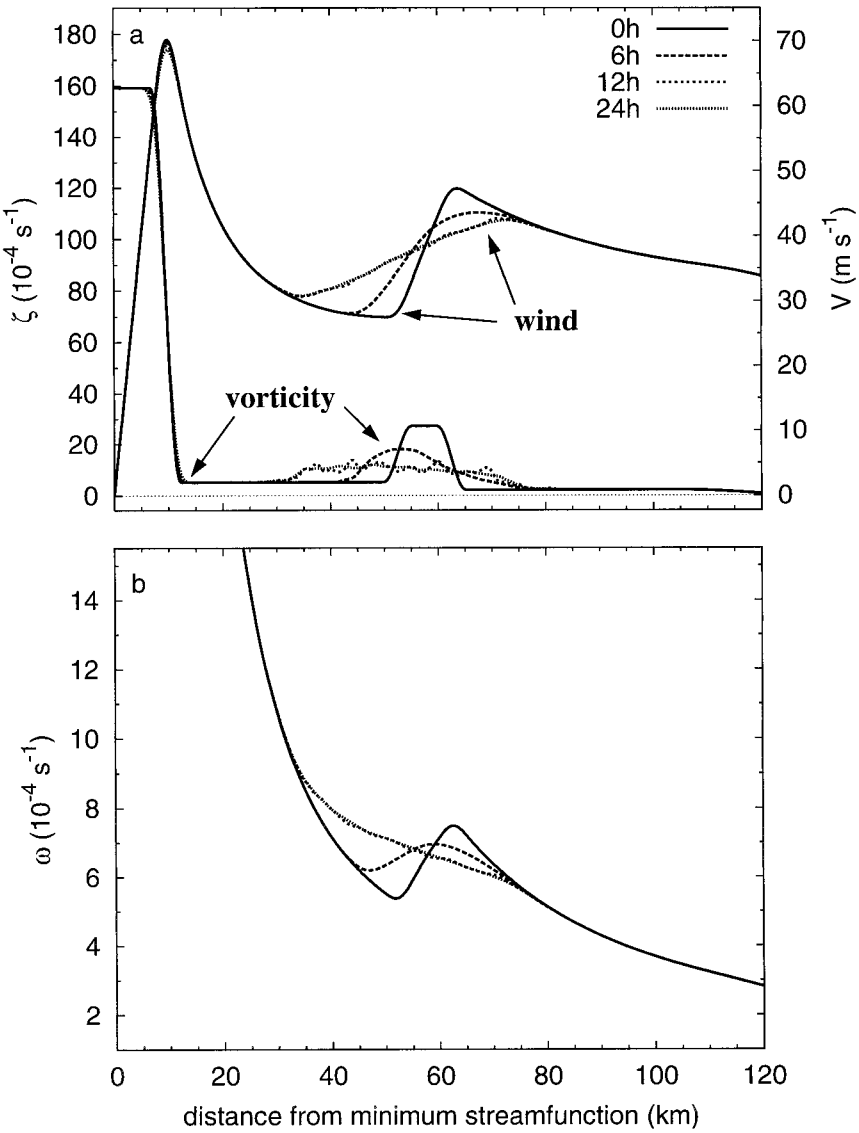

FIG. 4. (a) Azimuthal mean vorticity and tangential velocity, and (b) angular velocity for the experiment shown in Fig. 6 at the selected times $t = 0$ (solid), 6 h (long dash), 12 h (medium dash), and 24 h (short dash). Averages were computed with respect to distance from the minimum streamfunction position. The maximum angular velocity is truncated in the image to highlight the region of the annular ring. Note the reversal of differential rotation across the ring between 6 and 12 h.

km), the vortex helps to maintain the vorticity by inhibiting the growth of secondary instabilities across the thin strips.

At $t = 15$ h, the instabilities across the strips have rolled up into miniature vortices and during the remainder of the evolution to $t = 24$ h, these vortices undergo mixing and merger processes, relaxing the flow toward axisymmetry. Further time integration past $t = 24$ h results in little appreciable change other than a slow diffusive spindown.

The dashed lines of Fig. 4 show the evolution of the vorticity, tangential velocity, and angular velocity. The profiles represent azimuthal averages taken with respect to distance from the minimum streamfunction.[3] At $t = 6$ h, the annular ring has become broader and weaker and its maximum vorticity has moved inward. The tangential wind profile shows a weakening of the secondary maximum while the flow inside of the ring has strengthened, smoothing out the initially steep gradient between

[3] Although the centroid of vorticity on an f plane is invariant, asymmetries formed during the evolution cause the location of the minimum streamfunction to oscillate.

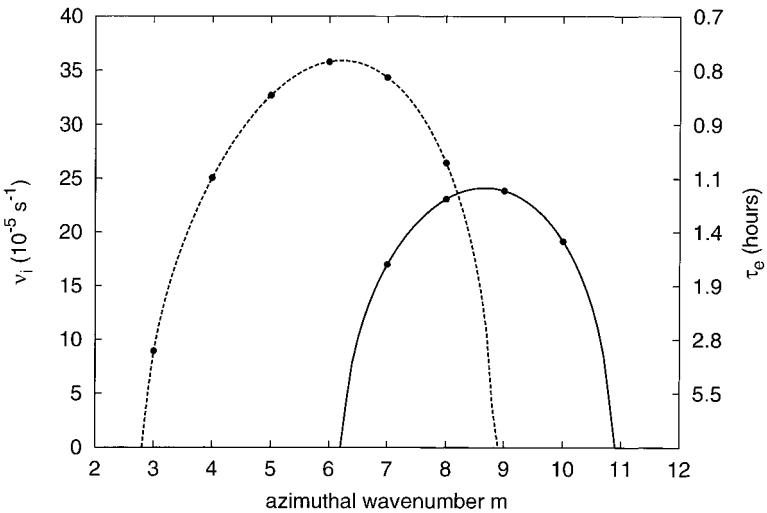

FIG. 5. Dimensional growth rates and *e*-folding times computed from Eq. (A6) for the piecewise uniform approximations to the initial conditions of sections 2c and 2d. The dots correspond to the integer values of azimuthal wavenumber *m*.

52 and 62 km. The angular velocity evolution exhibits a lessening of the differential rotation across the ring. At $t = 12$ h, the symmetric part of the flow has relaxed to a nearly steady state. The vorticity in the ring has further broadened and weakened but the secondary maximum and its associated gradient reversal have persisted. Similarly, the tangential wind maintains a significant secondary maximum with the flow increasing from 30 m s^{-1} at 35 km to 42 m s^{-1} at 73 km. The angular velocity has become monotonic, eliminating the positive differential rotation across the ring. Thus the symmetric part of the flow has become stable in the context of the four-region model, and little change is noted during the next 12 h.

The stability of the nearly equilibrated flow of the above experiment may offer insight into the observed longevity of hurricane secondary eyewalls. Our results are based on an initial condition that imitates a profile observed during a *single* radial flight leg into Hurricane Gilbert on 14 September 1988. This profile was chosen to demonstrate the mechanism whereby PV mixing can occur while still maintaining a secondary wind maximum. Black and Willoughby (1992) calculated *azimuthal mean* tangential wind profiles in Hurricane Gilbert based on aircraft observations at the beginning and end of the 14 September sortie (shown in their Fig. 4c). In the context of the four-region model, the mean profile at the beginning was found to be stable but near neutral, and the mean profile based on the flow near the end of the sortie was stable. Thus, the results of the experiment shown in Fig. 6 are useful in describing how an unstable secondary eyewall can evolve to a stable secondary eyewall, but these results could likely be an *exaggeration* of the actual evolution of a hurricane's secondary eyewall. It is possible that mixing associated with an unstable secondary eyewall is just enough to maintain a near-neutral flow.

d. Instability in the absence of a central vortex: Redistribution into a monopole

For comparison, a numerical simulation is performed with the central vortex removed, so that $\zeta_1 = \zeta_2 = 5.18 \times 10^{-4}$ s^{-1} and all other parameters in (11) remain essentially unchanged.[4] For further discussion of the evolution of unstable rings of enhanced vorticity without the presence of a central vortex, the reader is directed to Schubert et al. (1999). Radial profiles of the initial vorticity, tangential wind, and angular velocity fields are shown by the solid lines in Fig. 7. The differential rotation across the ring is greater than the previous example ($\omega \approx 3.1 \times 10^{-4}$ s^{-1} when $50 \leq r \leq 55$ km and $\omega \approx 5.3 \times 10^{-4}$ s^{-1} when $60 \leq r \leq 65$ km) and the maximum growth rate has shifted from wavenumber nine to six while the *e*-folding time has decreased from 67 to 48 min (dashed line in Fig. 5). The evolution is again displayed in the form of vorticity maps in Fig. 8.

At $t = 4$ h, the wavenumber-six maximum instability has amplified and a roll-up of the annular ring has occured. The presence of the wavenumber-seven instability, whose growth rate is 96% of the maximum instability, is evident in the northern quadrant. At $t = 8$ h, six well formed elliptical vortices have emerged. Weak vorticity from outside the ring is beginning to enter the

[4] The zero-circulation requirement of the doubly periodic domain results in a shift in the vorticity everywhere when any local change is made. Removing the central vortex causes a slight shift in ζ_2, ζ_3, ζ_4, ζ_5.

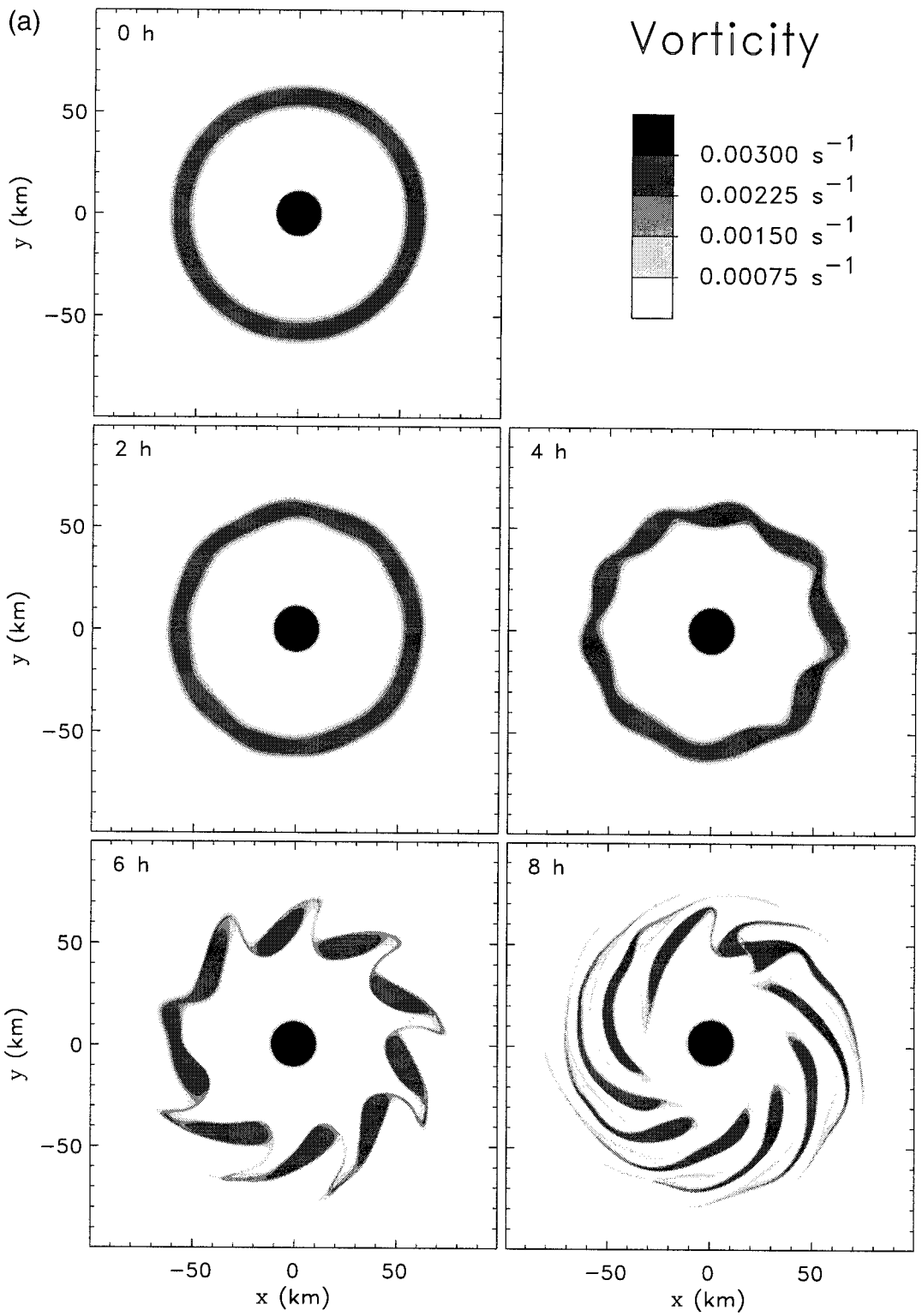

FIG. 6. Vorticity contour plots for the type 1 instability experiment. The model domain is 600 km × 600 km but only the inner 200 km × 200 km is shown. Successively darker shading denotes successively higher vorticity. Initially, high central vorticity is shaded black, enhanced vorticity in the ring is dark gray, and low vorticity in the moat and outside the eyewall is white. (a) $t = 0$ to $t = 8$ h. (b) $t = 10$ h to $t = 24$ h. The time interval switches from 2 to 3 h after $t = 12$ h.

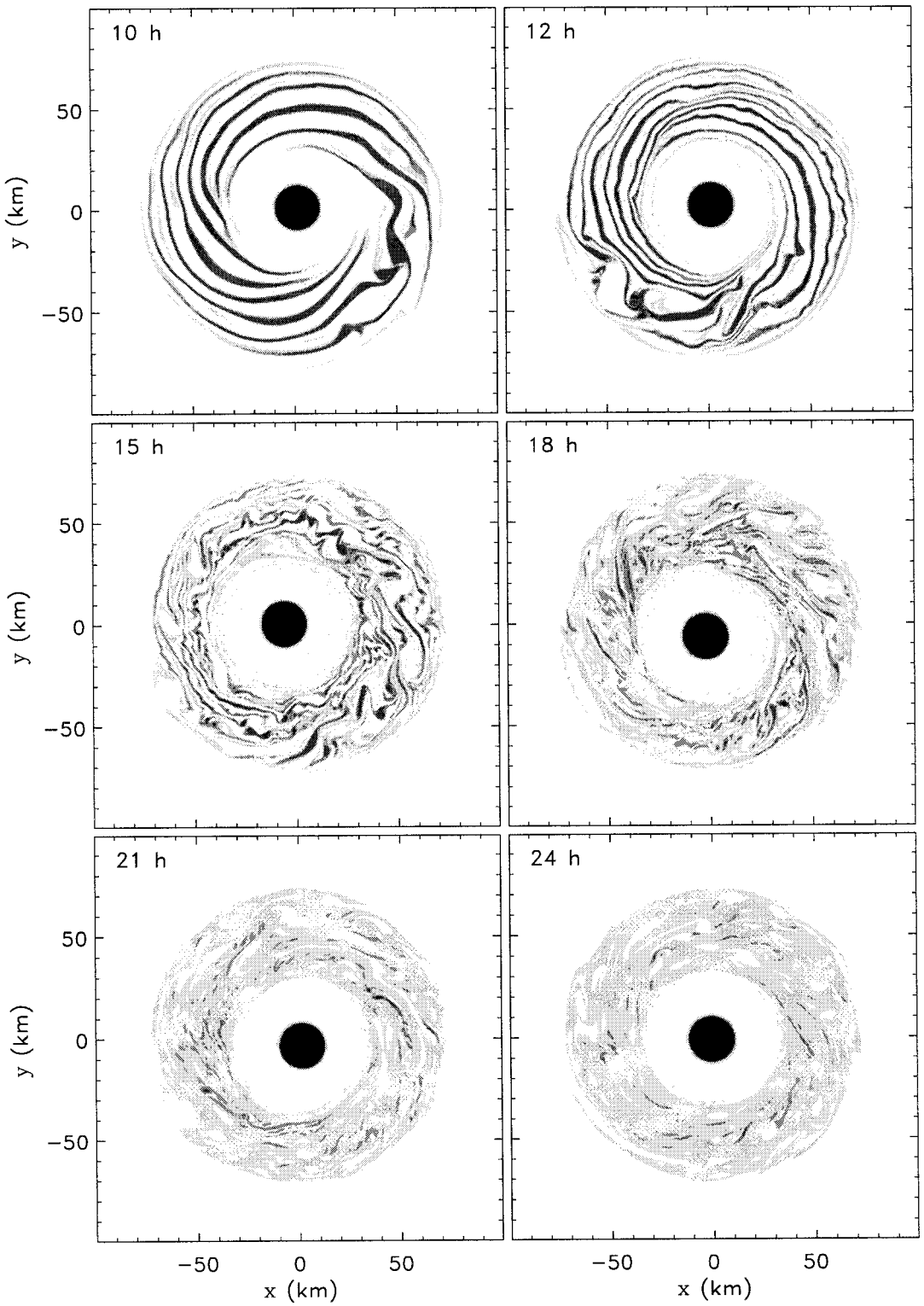

FIG. 6. (*Continued*)

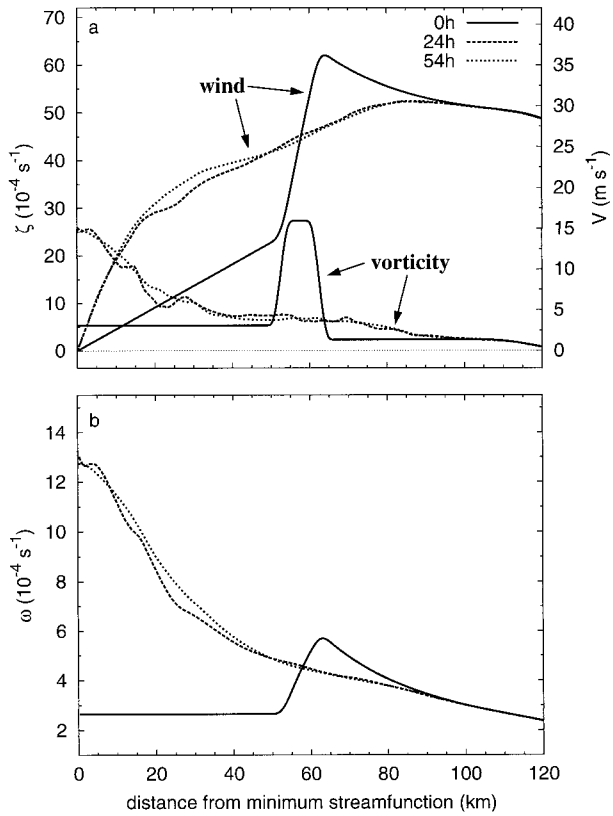

FIG. 7. Similar to Fig. 4 but for the experiment with the central vortex removed (shown in Fig. 8). The azimuthal mean vorticity profile when $t = 54$ h is monotonic.

central region of the vortex, while stronger vorticity from the center is ejected outward in the form of trailing spirals. After this time, intricate vortex merger and mixing processes dominate the evolution so that at $t = 16$ h, five vortices remain, and at $t = 24$ h, only three remain. Without the presence of a dominant central vortex, each coherent structure imposes a similar flow across the others. There is no clear victor in the merger process and high vorticity can mix to the center. At $t = 54$ h, the vorticity has nearly relaxed to a monotonic distribution that satisfies the Rayleigh sufficient condition for stability. This behavior is in marked contrast to the behavior in the presence of a central vortex (section 2c), where the mixing results in a monotonic angular velocity distribution which satisfies Fjørtoft's, but not Rayleigh's, sufficient condition for stability across the ring.

The vorticity rearrangement associated with type 1 instability suggests a nondivergent mechanism for the contraction of secondary eyewalls that may augment the axisymmetric contraction mechanism discussed by Shapiro and Willoughby (1982) and Willoughby et al. (1982). As part of an eyewall replacement cycle, the secondary eyewall strengthens through convergent and convective processes and as the secondary eyewall monopolizes the inflow of moist energy, the primary eyewall typically spins down. Both processes act to destabilize the secondary eyewall and result in asymmetric mixing that moves the inner edge of the secondary eyewall inward while the flow tends toward stability. As the secondary eyewall restrengthens, instabilities again emerge and the contraction process continues. As the primary eyewall weakens, the barrier to inward mixing is reduced until the mixing can reach the center, thus completing the cycle. In this case, the mechanisms that strengthen the secondary eyewall and weaken the primary eyewall rely largely on the divergent circulation but the contraction and ultimate replacement of the primary eyewall can be explained in terms of nondivergent asymmetric mixing processes alone.

3. Formation and persistence of an elliptical central vortex

Tropical cyclones sometimes have rotating elliptical eyes. Two outstanding examples were recently documented by Kuo et al. (1999) for the case of Typhoon Herb (1996), and by Reasor et al. (2000) for the case of Hurricane Olivia (1994). Typhoon Herb was observed using the WSR-88D radar on Wu-Feng Mountain in Taiwan. The elliptical eye of Typhoon Herb had an aspect ratio (major axis/minor axis) of approximately 1.5. Two complete rotations of the elliptical eye, each with a period of 144 min, were observed as the typhoon approached the radar. Kuo et al. interpreted this elliptical eye in terms of the Kirchhoff vortex (Lamb 1932, p. 232), an exact, stable (for aspect ratios less than 3) solution for two-dimensional incompressible flow having an elliptical patch of constant vorticity fluid surrounded by irrotational flow. Is the Kirchhoff vortex, with its discontinuous vorticity at the edge of the ellipse, a useful model of rotating elliptical eyes? Melander et al. (1987a) have shown that elliptical vortices with smooth transitions to the far-field irrotational flow are not robust but tend to become axisymmetrized via an inviscid process in which a halo of vorticity filaments become wrapped around a more symmetric vortex core. Montgomery and Kallenbach (1997) further clarified the physics of this process for initially monopolar distributions of basic-state vorticity, showing that axisymmetrization can be described as the radial and azimuthal dispersion of vortex Rossby waves that are progressively sheared by the differential rotation of the vortex winds. In this latter work, the dependence of the local wave frequency and stagnation radius on the radial vorticity gradient was made explicit. In other recent work, Koumoutsakos (1997) and Dritschel (1998) have shown that the extent to which a vortex axisymmetrizes is controlled by the steepness of the vortex edge, with very sharp initial vorticity distributions resulting in robust nonaxisymmetric configurations. This result is congruent with Kelvin's linear analysis for Rossby edge waves, in which the asymmetries never axisymmetrize on a

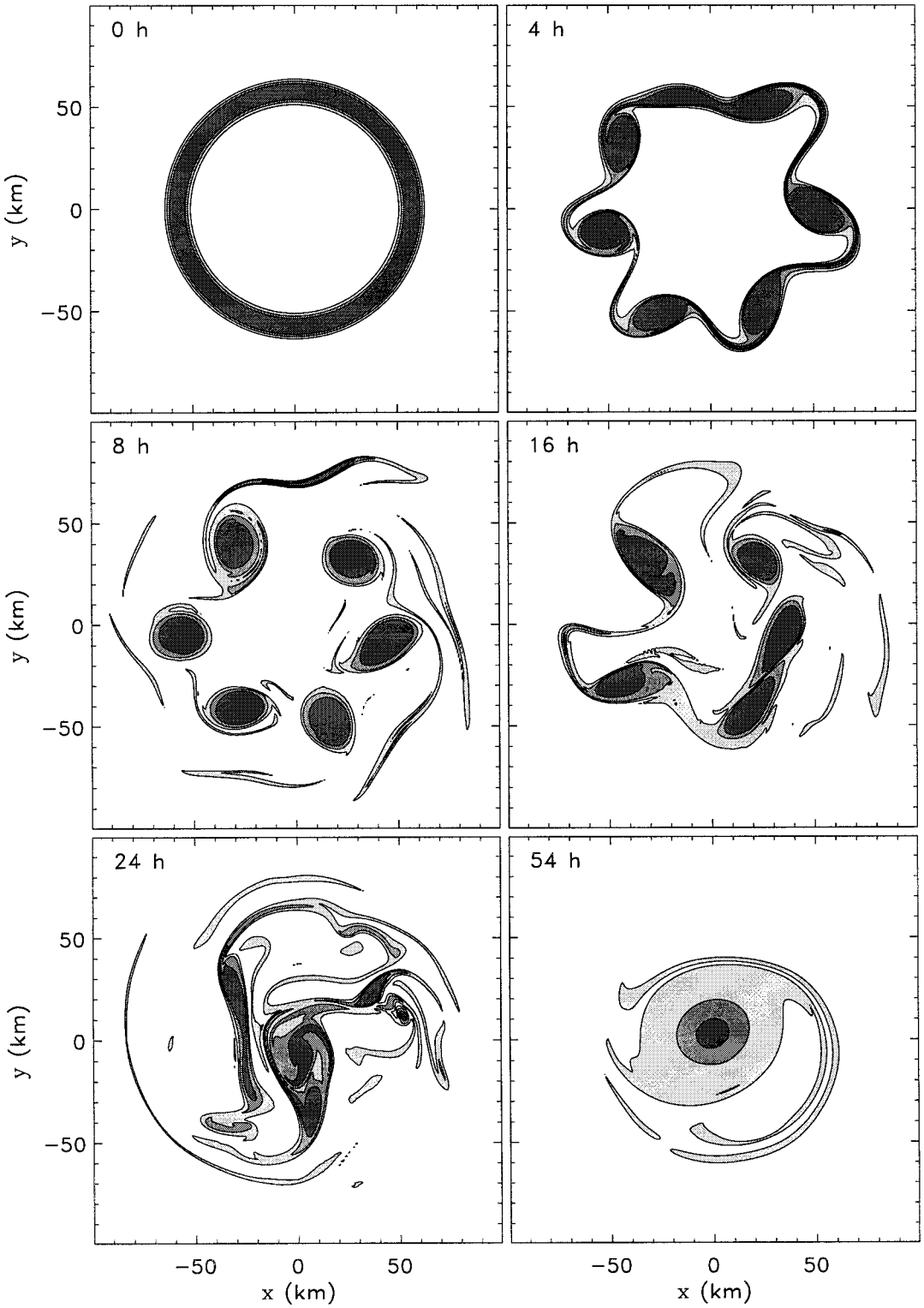

FIG. 8. Similar to the experiment of Fig. 6 but without the presence of the central vortex. The shading is the same as in Fig. 6. Plots are for the times t = 0, 4, 8, 16, 24, and 54 h.

discontinuous basic-state vorticity profile. If we now allow a sharp but smooth gradient, the local Wenzel–Kramers–Brillouin (WKB) theory of Montgomery and Kallenbach (1997) suggests radially trapped waves that axisymmetrize very slowly. The physics is generally a struggle between Rossby elasticity and radial shearing. Dritschel (1998, Figs. 6 and 7) gives an example of a robust, quasi-steady rotating elliptical pattern of vorticity with aspect ratio 1.6 in which approximately 40% of the vorticity drop from the center to the far field occurs discontinuously at the edge of the ellipse. A recent study by Montgomery and Enagonio (1998) further suggests that even in the absence of any discontinuity in a monotonic basic-state vorticity profile, convectively generated vortex Rossby waves can modify the basic state and cause a reversal in radial vorticity profile. The sign change allows for the existence of a discrete neutral or weakly unstable vortex Rossby mode that may not decay.

Reasor et al. (2000) documented the elliptical eyewall of Hurricane Olivia using NOAA WP-3D airborne dual-Doppler radar data and flight-level data, and identified barotropic instability across the eyewall as a possible source for the observed wavenumber-2 asymmetry. During the observation period, the symmetric part of the vorticity consisted of an elevated annular region within the eyewall surrounding a depressed region within the eye. An associated smooth basic-state vorticity profile was found to support instabilities with a maximum growth in wavenumber two. The observed wavenumber-2 vorticity asymmetry in the eyewall was hypothesized to be associated with the breakdown of an initially unstable ring of elevated vorticity as described by Schubert et al. (1999) and in section 2d of this study.

An alternative interpretation of the elliptical patterns observed in hurricanes is that their vorticity fields had evolved into structures resembling tripoles. Strictly speaking, a tripole is defined as a linear arrangement of three regions of distributed vorticity of alternate signs, with the whole configuration steadily rotating in the same sense as the vorticity of the elliptically shaped central core. Tripoles have been the subject of several laboratory experiments (Kloosterziel and van Heijst 1991; van Heijst et al. 1991; Denoix et al. 1994) and numerical simulations ever since they were shown to emerge as coherent structures in forced two-dimensional turbulence simulations (Legras et al. 1988). In addition to their emergence as coherent structures in two-dimensional turbulence, tripoles can be produced in a variety of ways, some quite exotic from the point of view of tropical cyclone dynamics. For example, tripoles can be produced by the collision of two asymmetric dipoles (Larichev and Reznik 1983) or by the offset collision of two symmetric Lamb dipoles (Orlandi and van Heijst 1992). Rossi et al. (1997) applied a quadrupolar distortion to a monopolar Gaussian vorticity distribution and found that for a large enough distortion, relaxation to a tripole can occur, demonstrating that finite-amplitude asymmetric perturbations applied to a stable monopole do not always relax to their axisymmetric base state. The generation mechanism of probable importance to tropical cyclone dynamics, however, is that associated with the barotropic instability of axisymmetric shielded or, more importantly, partially shielded[5] vortices (Gent and McWilliams 1986; Flierl 1988). Here we consider the central core of the vortex to be monotonic and, hence, eliminate possibly dominant instabilities that may occur across the eyewall, as investigated by Reasor et al. (2000).

a. Instability across the moat of a shielded vortex

A well-studied family of shielded monopoles has the angular velocity $\omega(r)$ given by

$$\omega(r) = \omega_0 \exp[-(r/b)^\alpha], \tag{13}$$

where ω_0 is the angular velocity at $r = 0$, b the size of the vortex, and α the steepness parameter, with $\alpha > 0$. The associated tangential wind $v(r) = r\omega(r)$ and vorticity $\zeta(r) = d(rv)/rdr$ are given by

$$v(r) = \omega_0 r \exp[-(r/b)^\alpha], \tag{14}$$

$$\zeta(r) = 2\omega_0\left[1 - \frac{1}{2}\alpha(r/b)^\alpha\right]\exp[-(r/b)^\alpha]. \tag{15}$$

Plots of ω/ω_0, $v/(b\omega_0)$, and $\zeta/(2\omega_0)$ as functions of r/b for $\alpha = 2, 3, 4, 5, 6$ are shown in Fig. 9. The radius of maximum tangential wind occurs at $r/b = (1/\alpha)^{1/\alpha}$, and the vorticity reverses sign at $r/b = (2/\alpha)^{1/\alpha}$ and is a minimum at $r/b = (1 + 2/\alpha)^{1/\alpha}$. Note that for increasing α, the vorticity in the core becomes more uniform, the annulus of negative $\zeta/(2\omega_0)$ becomes thinner and the vorticity gradient at the edge of the core becomes steeper. The instability and nonlinear evolution of this particular initial vorticity profile has been studied by Carton and McWilliams (1989), Carton et al. (1989), Orlandi and van Heijst (1992), Carton and Legras (1994), and Carnevale and Kloosterziel (1994). Carton and McWilliams (1989) showed that this vortex is linearly stable for $\alpha \lesssim 1.9$ and unstable for larger values of α. Carnevale and Kloosterziel (1994, their Fig. 7) showed that wavenumber two remains the fastest growing wave until $\alpha \approx 6$, at which point wavenumber three becomes the fastest growing wave. Within the range $1.9 < \alpha < 6$, the wavenumber-two instability can saturate as two distinct quasi-stable structures. Carton and Legras (1994) found that when $\alpha < 3.2$, saturation to a tripole occurs, while for $\alpha > 3.2$, two separating dipoles emerge. As α is increased, the nonlinear amplification

[5] An annular ring of negative vorticity can ''partially shield'' the far-field flow from a central core of positive vorticity just as, for example, in the element lithium (atomic number 3), the two electrons that occupy the inner, spherical 1*s*-orbital ''partially shield'' the outermost electron from the +3 charge of the nucleus.

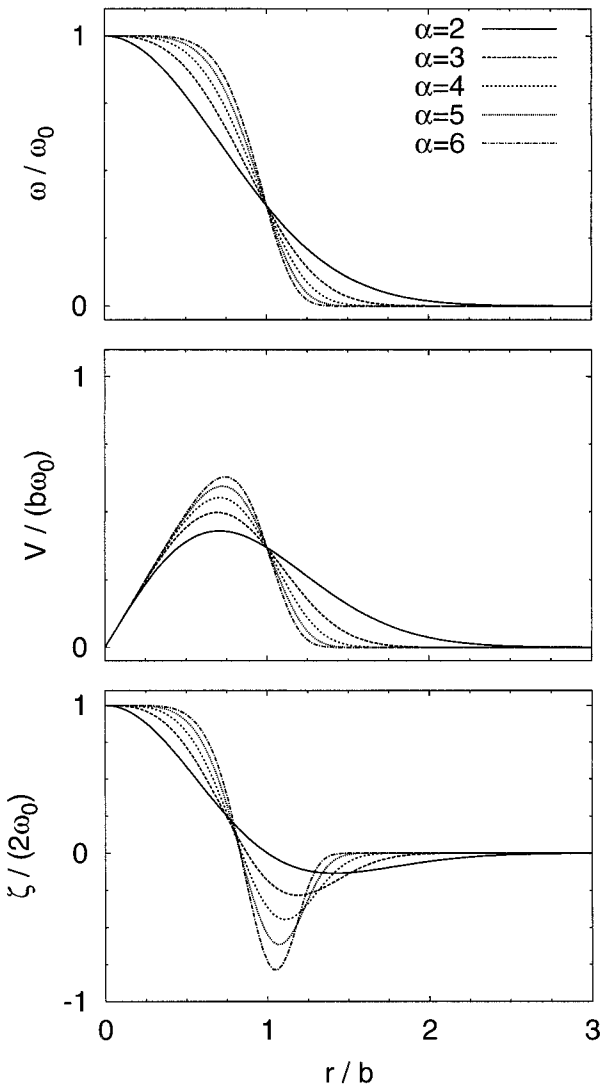

FIG. 9. Profiles of dimensionless angular velocity, tangential wind, and vorticity for unstable shielded monopoles. The maximum growth is in $m = 2$ when $\alpha = 2, 3, 4, 5$ and $m = 3$ when $\alpha = 6$. The profile is stable when $\alpha \leq 1.9$.

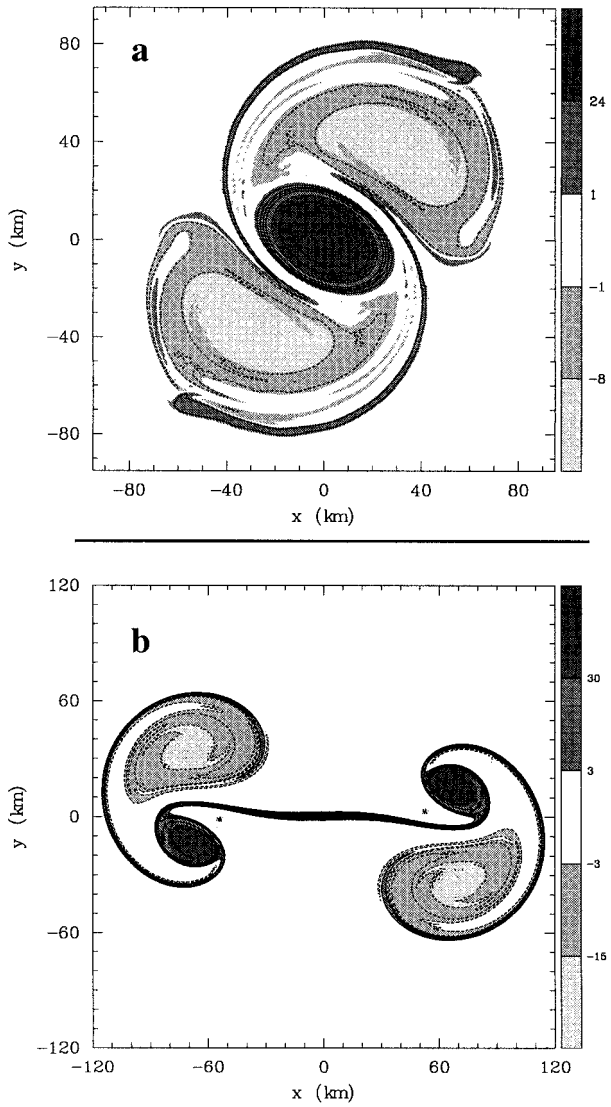

FIG. 10. (a) Saturation of a wavenumber-2 maximum instability to a tripole for a shielded monopole with $\alpha = 3$. The contours begin at -7×10^{-4} s^{-1} and are incremented by 5×10^{-4} s^{-1}. (b) Saturation to two separating dipoles when $\alpha = 4$. The contours begin at -15×10^{-4} s^{-1} and are incremented by 6×10^{-4} s^{-1}. The model domain for both plots is 600 km $\times$ 600 km, and values along the label bar are in units of 10^{-4} s^{-1}.

of wavenumber two increasingly elongates the central monopole, and when $\alpha > 3.2$, the central monopole is elongated to the point where it breaks as the two dipoles separate.

Two experiments are now performed using initial vorticity profiles given by (15) with $b = 35$ km and $\omega_0 = 1.85 \times 10^{-3}$ s^{-1}. For the first experiment, $\alpha = 3$ and for the second, $\alpha = 4$. In both experiments, an initial perturbation of proportional (1%) random noise is imposed across the moat.

When $\alpha = 3$, the wavenumber-two maximum instability results in a rearrangement of the vorticity into a tripole (Fig. 10a). During the early stages of the evolution, the central vorticity becomes highly elongated as the negative vorticity of the annulus is anticyclonically wrapped into two satellite vortices. The anticyclonic advection of the vorticity originally in the annulus is not due to the sign of the vorticity there, but is due to the arrangement of the positive vorticity being pulled from the central region. This will be more clearly demonstrated in section 3c. During the later stages, the aspect ratio (major axis/minor axis) of the elliptical central region has decreased to 1.7 with the satellite vortices found along the minor axis.

When $\alpha = 4$, the end result of the vorticity rear-

rangement is dramatically different. The wavenumber-two maximum instability does not saturate as a tripole but results in the formation of two separating dipoles (Fig. 10b). In the early part of the evolution, the negative vorticity within the moat is strong enough to elongate the central region into a strip and two pools of positive vorticity form within the strip near the two satellite vortices. The strip is eventually broken as the two dipoles propagate away from each other.

Since the radius of minimum vorticity is given by $r/b = (1 + 2/\alpha)^{1/\alpha}$, the evaluation of (15) at this radius yields the minimum vorticity $\zeta_{\min} = -\omega_0\alpha \exp[-(1 + 2/\alpha)]$, from which it is easily shown that $f + \zeta_{\min} < 0$ when $2\omega_0/f > (2/\alpha)\exp(1 + 2/\alpha)$. Thus, the minimum absolute vorticity is negative when $2\omega_0/f > 7.39$, 3.53, 2.24 for $\alpha = 2$, 3, 4 respectively. Recognizing that tropical cyclones have values of central vorticity exceeding 50 times the Coriolis parameter (i.e., $2\omega_0/f > 50$), the use of (13)–(15) as an initial condition in a full primitive equation model would result in regions of unrealistic negative inertial stability, that is, regions with $(f + 2v/r)(f + \zeta) < 0$. These considerations make application of the well-studied family of shielded monopoles (13)–(15) to tropical cyclones highly questionable. In section 3c, we will demonstrate that more realistic initial conditions, with positive vorticity in the moat, can also lead to the formation of tripoles.

b. *Linear stability analysis of a partially shielded vortex*

Returning to the four-region model of the appendix, consider the special case $\zeta_1 > 0$, $\zeta_2 < 0$, and $\zeta_3 = 0$. The axisymmetric basic-state angular velocity $\overline{\omega}(r)$ given by (A2) then reduces to

$$\overline{\omega}(r) = \frac{1}{2}\begin{cases}\zeta_1 & 0 \le r \le r_1,\\ [\zeta_1 r_1^2 + \zeta_2(r^2 - r_1^2)]r^{-2} & r_1 \le r \le r_2,\\ [\zeta_1 r_1^2 + \zeta_2(r_2^2 - r_1^2)]r^{-2} & r_2 \le r < \infty,\end{cases} \tag{16}$$

and the corresponding basic-state relative vorticity $\overline{\zeta}(r)$ given by (A3) reduces to

$$\overline{\zeta}(r) = \frac{d(r^2\overline{\omega})}{rdr} = \begin{cases}\zeta_1 & 0 < r < r_1,\\ \zeta_2 & r_1 < r < r_2,\\ 0 & r_2 < r < \infty,\end{cases} \tag{17}$$

where r_1, r_2 are specified radii and ζ_1, ζ_2 specified vorticity levels. The eigenvalue problem (A6) reduces to

$$\begin{bmatrix} m\overline{\omega}_1 + \frac{1}{2}(\zeta_2 - \zeta_1) & \frac{1}{2}(\zeta_2 - \zeta_1)(r_1/r_2)^m \\ -\frac{1}{2}\zeta_2(r_1/r_2)^m & m\overline{\omega}_2 - \frac{1}{2}\zeta_2 \end{bmatrix}\begin{pmatrix}\Psi_1\\ \Psi_2\end{pmatrix} = \nu\begin{pmatrix}\Psi_1\\ \Psi_2\end{pmatrix}. \tag{18}$$

Analogously to the discussion of section 2a, the system (18) describes the interaction between two counterpropagating vortex Rossby waves with the wave along the edge of the vortex ($r = r_1$) propagating clockwise relative to strong cyclonic flow, and the wave along the outer edge of the moat ($r = r_2$) propagating counterclockwise relative to weaker flow. In this case, both the Rayleigh and Fjørtoft necessary conditions for instability are satisfied. The eigenvalues of (18), normalized by ζ_1, are given by

$$\frac{\nu}{\zeta_1} = \frac{1}{4}\{m[1 + \zeta_2/\zeta_1 + (1 - \zeta_2/\zeta_1)(r_1/r_2)^2] - 1\} \pm \frac{1}{4}\langle\{m(1 - \zeta_2/\zeta_1)[1 - (r_1/r_2)^2] - [1 - 2(\zeta_2/\zeta_1)]\}^2 + 4(\zeta_2/\zeta_1)(1 - \zeta_2/\zeta_1)(r_1/r_2)^{2m}\rangle^{1/2}. \tag{19}$$

Figure 11 shows isolines of the imaginary part of ν/ζ_1 as a function of r_1/r_2 and $-\zeta_2/\zeta_1$. Although all basic states satisfy both the Rayleigh and Fjørtoft necessary conditions for instability, much of the region shown in Fig. 11 is stable, and for any value of $-\zeta_2/\zeta_1$, instability can occur only when $r_1/r_2 \gtrsim 0.38$. An interesting feature observed in Fig. 11 is that a larger central vortex is more susceptible to instability across its moat. For example, the secondary eyewall in Hurricane Gilbert on 14 September would need to contract to a radius less than 17 km in order for type 2 instability to occur. For the case of a larger central vortex ($r_1 = 30$ km) surrounded by a secondary eyewall where $-\zeta_2/\zeta_1$ is the same as the Gilbert case, type 2 instability occurs when the inner edge of the secondary eyewall contracts to a radius of 55 km.

c. *Type 2 instability across a moat of positive vorticity: Application to hurricanes*

The wind structure of a hurricane is intimately tied to the convective field, with the convection tending to produce low-level convergence and hence cyclonic vorticity in the area of a convective ring. When convection is concentrated near the inner edge of a ring of enhanced vorticity, a contraction of the ring may follow in response to nonconservative forcing (Shapiro and Willoughby 1982; Willoughby et al. 1982; Willoughby 1990). As the ring contracts, the differential rotation imposed across the ring by the central vortex becomes greater and eventually reverses the self-induced differential rotation of the ring. At this point, the ring is assured to have no type 1 instabilities. Further contraction, however, brings the inner edge of the ring closer to the central vortex where type 2 instabilities between the ring and central vortex can take place. Recalling Fig. 11 and noting that during a contraction, r_1/r_2 increases from small values toward unity, we expect type 2 instabilities to appear first with a maximum growth rate in wavenumber two. The vorticity mixing associ-

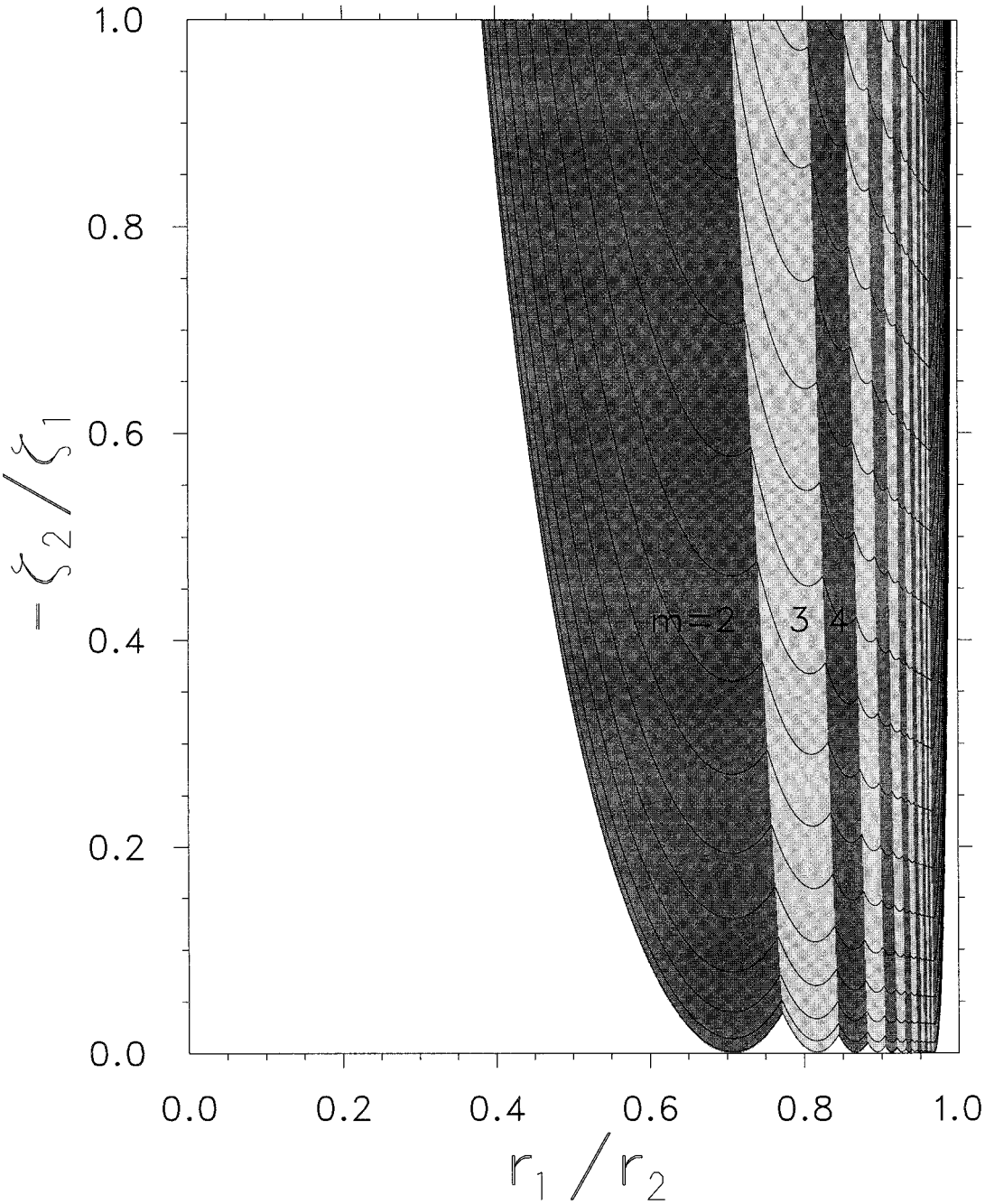

FIG. 11. Isolines of the maximum dimensionless growth rate ν_i/ζ_1 among the azimuthal wavenumbers $m = 3, 4, \ldots, 16$ for instability of a partially shielded vortex. The isolines and shading are the same as in Fig. 3.

ated with such an instability perturbs the vortex into a tripole and offers an explanation for the origin and persistence of elliptical eyewalls in hurricanes.

A numerical integration is now performed under the initial condition parameters $\{r_1, r_2, r_3, r_4\} = \{25, 40, 45, 67.5\}$ km, $\{d_1, d_2, d_3, d_4\} = \{2.5, 2.5, 2.5, 7.5\}$ km, and $\{\zeta_1, \zeta_2, \zeta_3, \zeta_4, \zeta_5\} = \{47.65, 1.15, 9.65, 1.15, -0.35\} \times 10^{-4}$ s^{-1}, which simulates a large central vortex of uniform vorticity surrounded by a thin ring of enhanced vorticity located at $r = 42.5$ km or 1.7 times the radius of maximum wind. The symmetric part of the initial vorticity and tangential wind fields are shown by the solid lines in Fig. 12. The secondary ring has the effect of flattening the tangential wind near $r = 42$ km but no secondary wind maximum is present. The retrograding vorticity waves along the central vortex

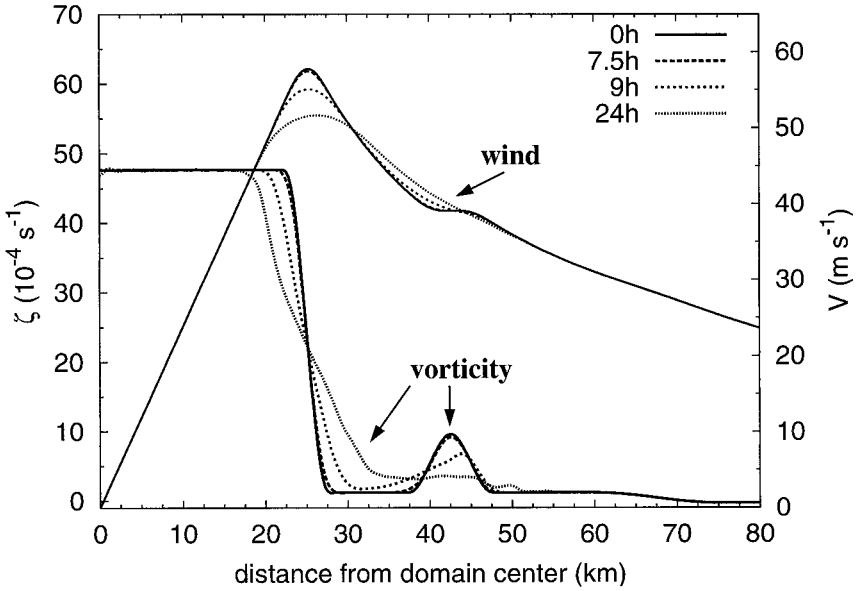

FIG. 12. Azimuthal mean vorticity and tangential velocity for the experiment shown in Fig. 13 at the selected times $t = 0$ (solid), 7.5 h (long dash), 9 h (medium dash), and 24 h (short dash).

edge ($r \approx 25$ km) are embedded in relatively strong angular velocity of 23.5×10^{-4} s^{-1} while the prograding waves along the inner edge of the ring ($r \approx 40$ km) are embedded in weaker angular velocity of 10.1×10^{-4} s^{-1}. Near the outer edge of the ring ($r \approx 45$ km), the angular velocity is 8.8×10^{-4} s^{-1}, suppressing type 1 instability. Solving (A6) for this basic state reveals a sole wavenumber-two instability whose growth rate has an *e*-folding time of 62 min. Results of this experiment are shown in Fig. 13.

At $t = 7.5$ h, the wavenumber-two instability becomes evident as the vortex and inner edge of the ring have been perturbed into ellipses. Asymmetries along the vortex are advected more quickly than those along the ring edge while the aspect ratios of the vortex and ring edge move farther away from unity, so that at $t = 9$ h, the major vertices of the vortex have moved close enough to the ring to begin stripping vorticity from it. The filaments of vorticity being stripped from the ring are then pulled across the moat into regions of stronger rotation and are advected along the vortex edge. As the leading edges of the filaments approach the downstream major vertices of the vortex, the differential rotation becomes greater and by $t = 10.5$ h, the outer edges of the filaments have become trailing features. As the trailing edges approach the downstream major vertices, their inner edges are again swept cyclonically along the edge of the vortex. At $t = 12$ h, this repetitive process has resulted in two strips of vorticity, which originated from the ring edge, wound anticyclonically around two pools of low vorticity, which originally composed the moat. The pools, or satellite vortices, lie along the minor axis of the elliptical central vortex. During its evolution, the central vortex takes on a variety of elliptical patterns with aspect ratios (major axis/minor axis) ranging from 1.3 to 1.8. Near the end of the simulation, the semimajor (semiminor) axis is near 60 km (40 km) giving an aspect ratio near 1.5. Although the ellipticity of the central vortex is a persistent feature, the tripole pattern becomes less easily identified when $t > 12$ h as the vorticity of the ring becomes increasingly mixed into the regions of the satellites.

The period of rotation of the tripole is approximately 89 min. The linear theory of Kelvin (Lamb 1932, 230–231) applied to a wavenumber-two asymmetry on a Rankine vortex with $V_{\max} = 58$ m s^{-1} at $r = 25$ km predicts a period of rotation of 90 min. The good agreement between Kelvin's theory and the model results suggest that the period of rotation of a tripole can be predicted well if treated as a Kirchhoff vortex and is then in good agreement with the results of Kuo et al. (1999). Polvani and Carton (1990) calculated the rotation rate of a point-vortex tripole using the formula

$$\Omega = \frac{1}{2\pi d^2}\left(\Gamma_1 + \frac{\Gamma_2}{2}\right), \tag{20}$$

where d is the distance from the centroid of the elliptical central vortex to the centroid of either satellite vortex and Γ_1, Γ_2 are the circulations of the central and satellite vortices. It is not clear how to accurately apply (20) to our numerical results since the calculation of Γ_2 requires quantification of how much vorticity from the ring has been wound around the low vorticity of the moat. We

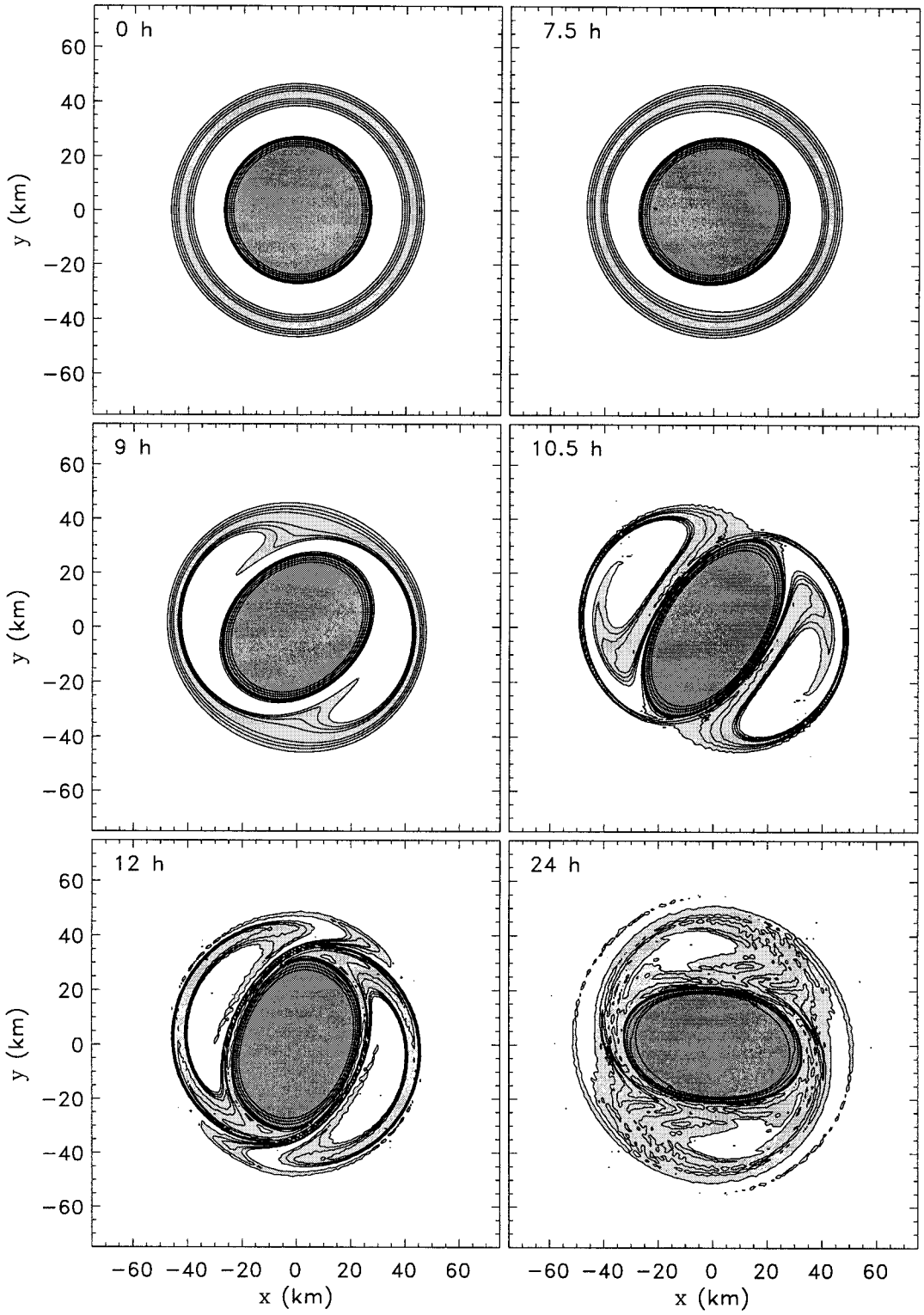

FIG. 13. Vorticity contour plots for the type 2 instability experiment. Selected times are $t = 0$, 7.5, 9, 10.5, 12, and 24 h. Successively darker shading denotes successively higher vorticity.

can, however, approximate a range of values between two extreme cases, one in which the satellite vortices contain only vorticity from the moat, and the other in which the satellite vortices have ingested all of the vorticity of the ring. At 24 h the centroid of each satellite vortex is roughly 36 km from the centroid of the central vortex and we can assume that the circulation of the central vortex has remained nearly fixed so that $\Gamma_1 \approx 2.98\pi$ km^2 s^{-1}. If no vorticity from the ring were ingested by the satellite vortices, then their circulations would be half the initial circulation of the moat, yielding $\Gamma_2 \approx 0.06\pi$ km^2 s^{-1}. If all of the ring vorticity were ingested by the satellite vortices, then their circulations would be half the sum of the initial circulations of the moat and ring, yielding $\Gamma_2 \approx 0.26\pi$ km^2 s^{-1}. Using these values in (20) we obtain the range of rotation periods $87 \lesssim P \lesssim 90$ min, where $P = 2\pi/\Omega$. It is clear that in this case, where $\Gamma_1 \gg \Gamma_2$, there is little sensitivity to the choice of Γ_2 and the accuracy of (20) depends largely on the estimated value of d.

The evolution of the symmetric part of the flow (dashed lines in Fig. 12) shows a 26% reduction of the maximum vorticity in the ring during the initial stage of the tripole formation between $t = 7.5$ h and $t = 9$ h. This reduction smooths out the wind profile with the initial flat spot replaced with a more uniform slope. At $t = 24$ h, the vorticity has become nearly monotonic except for a small bump near $r = 50$ km where trailing spirals are present, and the tangential wind maximum has decreased from its initial value of 58 to 52 m s^{-1}. A remarkable aspect of type 2 instability is that a large and intense central vortex can be dramatically perturbed by apparently undramatic features of its near environment. For example, a thin ring of vorticity that is stabilized by its proximity to a central vortex can persist indefinitely but is barely discernable in the wind field. Any subsequent strengthening or contraction of the ring can introduce type 2 instability, and the central vortex would be significantly rearranged.

Unlike the case of an initial shielded vortex (section 3a), where wavenumber-two instabilities can saturate as tripoles or dipole pairs, the emergence of a tripole in our numerical simulations appears to be an ubiquitous result of type 2 instability across a moat of reduced, but positive vorticity. Tripoles result from a variety of initial conditions that share the common feature of a depressed region of vorticity within the moat, with higher vorticity outside. The initial width of the annular ring of elevated vorticity is unimportant to the early development of a tripole since the outer edge of the ring is dynamically inactive. The width of the ring does, however, play a role in the flow evolution at later times. As seen in the numerical results of Fig. 14, for the case of an initially broad annular ring, the formation of a tripole is followed by a relaxation to a nearly steady solid body rotation that is absent in the previous experiment. In this case, most of the vorticity within the interior of the ring does not participate in the vorticity rearrangement and the tripole pattern is more robust.

The observational signature of a tripolar structure would likely be identified by the presence of its weak satellite vortices, but the position where the satellites would be expected to reside may inhibit such identification. For example, airborne Doppler radar–derived flows, as calculated by Reasor et al. (2000), can become suspect at distances greater than 30–40 km from the hurricane center. In the experiment shown in Fig. 13, the satellite vortices reside near $r = 40$ km. The presence of such satellites in an actual hurricane could then be difficult to identify without some modification to present airborne radar-based methods.

4. Concluding remarks

The relative importance of conservative vorticity dynamics in a mature hurricane, compared with the nonconservative effects of friction and moist convection, is an open question. Ideally, the hurricane should be simulated using a progression of numerical models of varying complexity. Working from the nonhydrostatic primitive equations to the nondivergent barotropic model, the implications of each simplification can be measured in terms of the question ''what physics remain?'' while progressing in the opposite sense, the question ''what physics are introduced?'' must be addressed. With more complex models, fundamental mechanisms may be obscured by the inclusion of additional but extraneous dynamics that often require parameterizations and typically must compromise, sometimes severely, numerical resolution and thus dynamical accuracy. With simpler models, there exists the danger that apparently dominant mechanisms would be completely overshadowed by the inclusion of additional physics.

The present study was confined to the simple framework of the nondivergent barotropic model in an attempt to capture the fundamental interaction between a hurricane primary eyewall and surrounding regions of enhanced vorticity in the context of asymmetric PV redistribution. A four-region model was used to simulate a monopolar central vortex surrounded by a region of low vorticity, or moat, which in turn was surrounded by an annular ring of enhanced vorticity. The moat was found to be a region of intense differential rotation and associated enstrophy cascade where cumulonimbus convection would have difficulty persisting. This mechanism offered an additional explanation beyond mesoscale subsidence for the relative absence of deep convection in the moat.

The four-region model provided a basic state that can support two instability types. In the first instability type, phase locking occured between vortex Rossby waves propagating along the inner and outer edges of the annular ring. The central vortex was dynamically inactive but served to induce a differential rotation across the ring, which had the effect of stabilizing the ring by

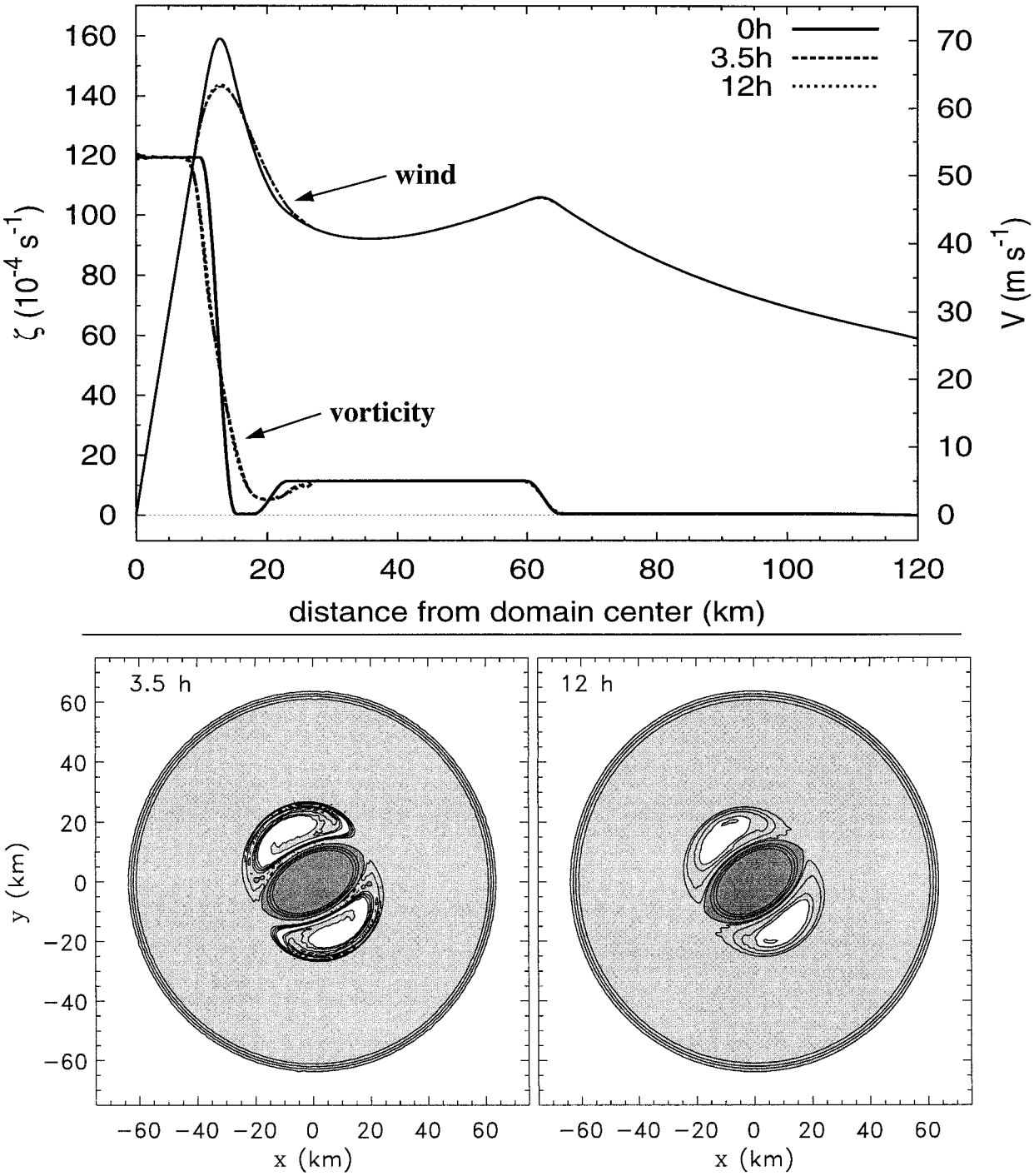

FIG. 14. Results of the numerical integration for the case of an initially wide annular ring. Mean profiles of vorticity and tangential wind and vorticity contour plots for $t = 3.5$ h and $t = 12$ h. The outer edge of the ring does not participate in the mixing and the tripole rotates nearly as a solid body. Little change is observed in the mean profiles after $t = 3.5$ h.

opposing its self-induced differential rotation and inhibiting phase locking between the ring edges. This stabilizing mechanism offered an explanation for the observed longevity of secondary eyewalls in hurricanes. Observed mean profiles in Hurricane Gilbert, calculated by Black and Willoughby (1992), suggested that the presence of Gilbert's central vortex was indeed adequate to stabilize its secondary eyewall. In the case where the

opposing differential rotation was insufficient to completely stabilize the ring, the vorticity of the ring mixed to form a broader and weaker ring. During this process, the central vortex imposed a barrier to inward mixing and inhibited rearrangement into a monopole. The flow relaxed to a quasi-steady state, which satisfied the Fjørtoft sufficient condition for stability while still satisfying the Rayleigh necessary condition for instability, and while maintaining a significant secondary wind maximum.

In the second instability type, the outer edge of the annulus was rendered dynamically inactive by the vortex-induced differential rotation, and interaction across the moat between the inner edge of the annular ring and the outer edge of the central vortex took place. This instability was most likely realized in azimuthal wavenumber two and the subsequent mixing resulted in the formation of a tripole. This mechanism offered an explanation for the origin and persistence of elliptical eyewalls, but the existence and significance of type 2 instabilities in tropical cyclones remains an open question.

Acknowledgments. The authors would like to thank Rick Taft, Paul Reasor, Scott Fulton, William Gray, John Knaff, Mark DeMaria, Frank Marks, Peter Dodge, Mel Nicholls, and Hung-Chi Kuo for many helpful comments and discussions. This work was supported by NSF Grant ATM-9729970 and by NOAA Grant NA67RJ0152 (Amendment 19).

APPENDIX

Linear Stability Analysis of the Four-Region Model

Consider a circular basic-state vortex whose angular velocity $\overline{\omega}(r)$ is a given function of radius r. Using cylindrical coordinates (r, ϕ), assume that the small-amplitude perturbations of the streamfunction, $\psi'(r, \phi, t)$, are governed by the linearized barotropic nondivergent vorticity equation $(\partial/\partial t + \overline{\omega}\partial/\partial\phi)\nabla^2\psi' - (\partial\psi'/r\partial\phi)(d\overline{\zeta}/dr) = 0$, where $\overline{\zeta}(r) = d(r^2\overline{\omega})/rdr$ is the basic-state relative vorticity, $(u', v') = (-\partial\psi'/r\partial\phi, \partial\psi'/\partial r)$ the perturbation radial and tangential components of velocity, and $\partial(rv')/r\partial r - \partial u'/r\partial\phi = \nabla^2\psi'$ the perturbation vorticity. Searching for modal solutions of the form $\psi'(r, \phi, t) = \hat{\psi}(r)e^{i(m\phi - \nu t)}$, where m is the azimuthal wavenumber and ν the complex frequency, we obtain the radial structure equation

$$(\nu - m\overline{\omega})\left[r\frac{d}{dr}\left(r\frac{d\hat{\psi}}{dr}\right) - m^2\hat{\psi}\right] + mr\frac{d\overline{\zeta}}{dr}\hat{\psi} = 0. \quad \text{(A1)}$$

A useful idealization of an annular region of elevated vorticity surrounding a central vortex is the piecewise constant four region model. In this model the axisymmetric basic-state angular velocity $\overline{\omega}(r)$ is given by

$$\overline{\omega}(r) = \frac{1}{2}\begin{cases}\zeta_1 & 0 \le r \le r_1,\\ \zeta_2 - (\zeta_2 - \zeta_1)(r_1/r)^2 & r_1 \le r \le r_2,\\ \zeta_3 - (\zeta_2 - \zeta_1)(r_1/r)^2 - (\zeta_3 - \zeta_2)(r_2/r)^2 & r_2 \le r \le r_3,\\ -(\zeta_2 - \zeta_1)(r_1/r)^2 - (\zeta_3 - \zeta_2)(r_2/r)^2 + \zeta_3(r_3/r)^2 & r_3 \le r < \infty,\end{cases} \quad \text{(A2)}$$

and the corresponding basic-state relative vorticity by

$$\overline{\zeta}(r) = \frac{d(r^2\overline{\omega})}{rdr} = \begin{cases}\zeta_1 & 0 < r < r_1,\\ \zeta_2 & r_1 < r < r_2,\\ \zeta_3 & r_2 < r < r_3,\\ 0 & r_3 < r < \infty,\end{cases} \quad \text{(A3)}$$

where r_1, r_2, r_3 are specified radii and ζ_1, ζ_2, ζ_3 are specified vorticity levels.

Restricting study to the class of perturbations whose disturbance vorticity arises solely through radial displacement of the basic-state vorticity, then the perturbation vorticity vanishes everywhere except near the edges of the constant vorticity regions, that is, (A1) reduces to $(rd/dr)(rd\hat{\psi}/dr) - m^2\hat{\psi} = 0$ for $r \neq r_1, r_2, r_3$. The general solution of this equation in the four regions separated by the radii r_1, r_2, r_3 can be constructed from different linear combinations of r^m and r^{-m} in each region. A physically revealing approach is to write the general solution, valid in any of the four regions, as a linear combination of the basis functions $B_j^{(m)}(r)$, defined by

$$B_j^{(m)}(r) = \begin{cases}(r/r_j)^m & 0 \le r \le r_j,\\ (r_j/r)^m & r_j \le r < \infty,\end{cases} \quad \text{(A4)}$$

for $j = 1, 2, 3$. The solution for $\hat{\psi}(r)$ is then $\hat{\psi}(r) = \Psi_1 B_1^{(m)}(r) + \Psi_2 B_2^{(m)}(r) + \Psi_3 B_3^{(m)}(r)$, where Ψ_1, Ψ_2, and Ψ_3 are complex constants. Since $dB_1^{(m)}/dr$ is discontinuous at $r = r_1$, the solution associated with the constant Ψ_1 has vorticity anomalies concentrated at $r = r_1$ and the corresponding streamfunction decays away in both directions from $r = r_1$. Similarly, the solutions associated with the constants Ψ_2 and Ψ_3 have vorticity

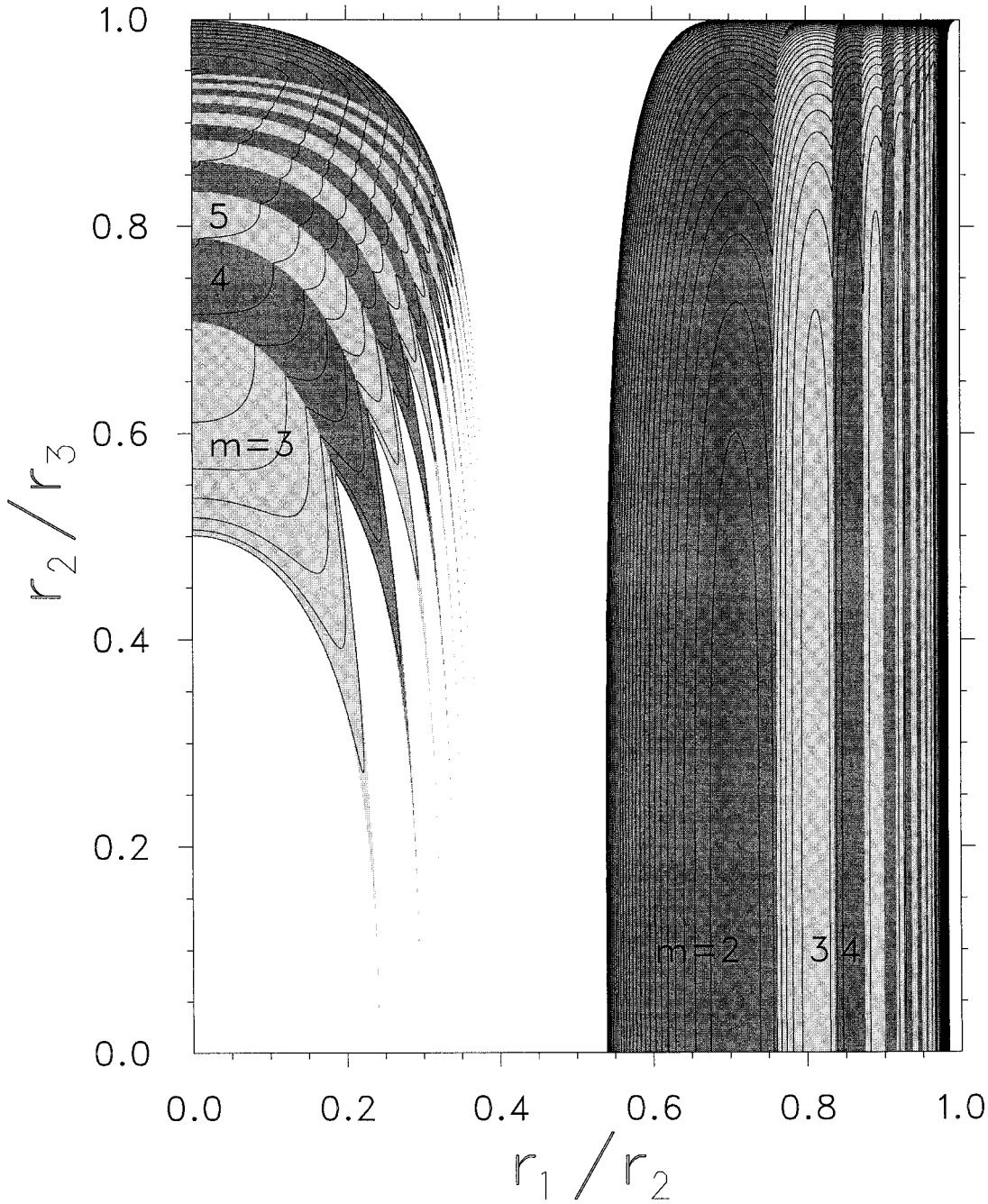

FIG. A1. Isolines of the maximum value of the dimensionless growth rate ν_i/ζ_3, computed from (A7), as a function of r_1/r_2 and r_2/r_3 for the case $\zeta_1/\zeta_3 = 5.7$ and for azimuthal wavenumbers up to $m = 16$. Type 1 instability (for $m = 3, 4, \ldots, 16$) occurs on the left side of the diagram and type 2 instability (for $m = 2, 3, \ldots, 16$) occurs on the right side. The azimuthal wavenumber associated with the most unstable mode is indicated by the alternating gray scales. The white region is stable, and the isolines are $\nu_i/\zeta_3 = 0.01, 0.03, 0.05, \ldots$.

anomalies concentrated at $r = r_2$ and $r = r_3$, respectively.

In order to relate Ψ_1, Ψ_2, Ψ_3, we integrate (A1) over the narrow radial intervals centered at r_1, r_2, r_3 to obtain the jump (pressure continuity) conditions

$$\lim_{\epsilon\to 0}\left[(\nu - m\overline{\omega}_j)r_j\left(\frac{d\hat{\psi}}{dr}\right)_{r_j-\epsilon}^{r_j+\epsilon}\right] + (\zeta_{j+1} - \zeta_j)m\hat{\psi}(r_j) = 0, \tag{A5}$$

where $\overline{\omega}_j = \overline{\omega}(r_j)$ and $j = 1, 2, 3$. Substituting our general solution into the jump conditions (A5) yields the matrix eigenvalue problem

$$\begin{pmatrix} m\overline{\omega}_1 + \frac{1}{2}(\zeta_2 - \zeta_1) & \frac{1}{2}(\zeta_2 - \zeta_1)(r_1/r_2)^m & \frac{1}{2}(\zeta_2 - \zeta_1)(r_1/r_3)^m \\ \frac{1}{2}(\zeta_3 - \zeta_2)(r_1/r_2)^m & m\overline{\omega}_2 + \frac{1}{2}(\zeta_3 - \zeta_2) & \frac{1}{2}(\zeta_3 - \zeta_2)(r_2/r_3)^m \\ -\frac{1}{2}\zeta_3(r_1/r_3)^m & -\frac{1}{2}\zeta_3(r_2/r_3)^m & m\overline{\omega}_3 - \frac{1}{2}\zeta_3 \end{pmatrix} \begin{pmatrix} \Psi_1 \\ \Psi_2 \\ \Psi_3 \end{pmatrix} = \nu \begin{pmatrix} \Psi_1 \\ \Psi_2 \\ \Psi_3 \end{pmatrix}. \quad \text{(A6)}$$

Noting that for the basic state given by (A2), $\overline{\omega}_1 = \frac{1}{2}\zeta_1$, $\overline{\omega}_2 = \frac{1}{2}[\zeta_2 - (\zeta_2 - \zeta_1)(r_1/r_2)^2]$ and $\overline{\omega}_3 = \frac{1}{2}[\zeta_3 - (\zeta_2 - \zeta_1)(r_1/r_3)^2 - (\zeta_3 - \zeta_2)(r_2/r_3)^2]$, we can solve the eigenvalue problem (A6) once we have specified the parameters m, r_1, r_2, r_3, ζ_1, ζ_2, ζ_3.

Now consider the special case obtained by assuming $\zeta_2 = 0$. Then, dividing the first row of (A6) by $\frac{1}{2}\zeta_1$ and the second and third rows by $\frac{1}{2}\zeta_3$, we obtain

$$\begin{vmatrix} 1 - m + 2\left(\frac{\zeta_1}{\zeta_3}\right)^{-1}\left(\frac{\nu}{\zeta_3}\right) & \left(\frac{r_1}{r_2}\right)^m & \left(\frac{r_1}{r_3}\right)^m \\ \left(\frac{r_1}{r_2}\right)^m & 1 + m\left(\frac{\zeta_1}{\zeta_3}\right)\left(\frac{r_1}{r_2}\right)^2 - 2\left(\frac{\nu}{\zeta_3}\right) & \left(\frac{r_2}{r_3}\right)^m \\ \left(\frac{r_1}{r_3}\right)^m & \left(\frac{r_2}{r_3}\right)^m & 1 - m\left[1 + \frac{\zeta_1}{\zeta_3}\left(\frac{r_1}{r_3}\right)^2 - \left(\frac{r_2}{r_3}\right)^2\right] + 2\left(\frac{\nu}{\zeta_3}\right) \end{vmatrix} = 0. \quad \text{(A7)}$$

For given r_1/r_2, r_2/r_3, and ζ_1/ζ_3, the determinant (A7) yields three values of the dimensionless frequency ν/ζ_3. Choosing the most unstable of these three roots, Fig. A1 shows isolines of the imaginary part of ν/ζ_3 as a function of r_1/r_2 and r_2/r_3 for the case $\zeta_1/\zeta_3 = 5.7$. For this value of ζ_1/ζ_3, there are two distinct types of instability. Type 1 occurs for azimuthal wavenumbers $m = 3, 4, 5, \ldots$ when r_1 is small compared to r_2 and when r_2 is nearly as large as r_3 (the annular ring of elevated vorticity is narrow). Type 1 instability involves the interaction of vorticity waves at r_2 and r_3, that is, across the ring of elevated vorticity. Type 2 instability occurs for azimuthal wavenumbers $m = 2, 3, 4, \ldots$ when r_1 is nearly as large as r_2 (the moat is narrow). Type 2 instability involves the interaction of vorticity waves at r_1 and r_2, that is, across the moat. Although the two types of instability are well separated when $\zeta_1/\zeta_3 = 5.7$ (and larger), they begin to overlap in the central part of the diagram as ζ_1/ζ_3 decreases to approximately 2. Type 1 instability is discussed in section 2 and type 2 instability in section 3.

The analysis presented here is an extension of previous work by Dritschel (1989) and Carton and Legras (1994). Dritschel considered the thin-strip limit $r_2 - r_1 \gg r_3 - r_2$, where instabilities across the ring strongly dominate instabilities across the moat. The region of Fig. A1 that is pertinent in this limit is restricted to the upper-left corner and, in this case, instabilities that serve as a precursor to tripole formation are suppressed. Carton and Legras considered the special case of the four-region model applied to shielded monopoles. They present solutions to the eigenvalue problem (A7) where the vorticity of the ring is restricted to be negative and given by $\zeta_3 = -\zeta_1[r_1^2/(r_3^2 - r_2^2)]$.

REFERENCES

Black, M. L., and H. E. Willoughby, 1992: The concentric eyewall cycle of Hurricane Gilbert. *Mon. Wea. Rev.*, **120,** 947–957.

Carnevale, G. F., and R. C. Kloosterziel, 1994: Emergence and evolution of triangular vortices. *J. Fluid Mech.*, **259,** 305–331.

Carr, L. E., III, and R. T. Williams, 1989: Barotropic vortex stability to perturbations from axisymmetry. *J. Atmos. Sci.*, **46,** 3177–3191.

Carton, X. J., and B. Legras, 1994: The life-cycle of tripoles in two-dimensional incompressible flows. *J. Fluid Mech.*, **267,** 53–82.

——, and J. C. McWilliams, 1989: Barotropic and baroclinic instabilities of axisymmetric vortices in a quasi-geostrophic model. *Mesoscale/Synoptic Coherent Structures in Geophysical Tur-*

bulence, J. C. J. Nihoul and B. M. Jamart, Eds., Elsevier, 339–344.

——, G. R. Flierl, and L. M. Polvani, 1989: The generation of tripoles from unstable axisymmetric isolated vortex structures. *Europhys. Lett.,* **9,** 339–344.

Denoix, M.-A., J. Sommeria, and A. Thess, 1994: Two-dimensional turbulence: The prediction of coherent structures by statistical mechanics. *Progress in Turbulence Research,* H. Branover and Y. Unger, Eds., AIAA, 88–107.

Dodge, P., R. W. Burpee, and F. D. Marks Jr., 1999: The kinematic structure of a hurricane with sea level pressure less than 900 mb. *Mon. Wea. Rev.,* **127,** 987–1004.

Dritschel, D. G., 1989: On the stabilization of a two-dimensional vortex strip by adverse shear. *J. Fluid Mech.,* **206,** 193–221.

——, 1998: On the persistence of non-axisymmetric vortices in inviscid two-dimensional flows. *J. Fluid Mech.,* **371,** 141–155.

——, and D. W. Waugh, 1992: Quantification of the inelastic interaction of unequal vortices in two-dimensional vortex dynamics. *Phys. Fluids A,* **4,** 1737–1744.

Flierl, G. R., 1988: On the instability of geostrophic vortices. *J. Fluid Mech.,* **197,** 349–388.

Gent, P. R., and J. C. McWilliams, 1986: The instability of barotropic circular vortices. *Geophys. Astrophys. Fluid Dyn.,* **35,** 209–233.

Kloosterziel, R. C., and G. J. F. van Heijst, 1991: An experimental study of unstable barotropic vortices in a rotating fluid. *J. Fluid Mech.,* **223,** 1–24.

Koumoutsakos, P., 1997: Inviscid axisymmetrization of an elliptical vortex. *J. Comput. Phys.,* **138,** 821–857.

Kuo, H.-C., R. T. Williams, and J.-H. Chen, 1999: A possible mechanism for the eye rotation of Typhoon Herb. *J. Atmos. Sci.,* **56,** 1659–1673.

Lamb, H., 1932: *Hydrodynamics.* 6th ed. Cambridge University Press, 738 pp.

Larichev, V. D., and G. M. Reznik, 1983: On collisions between two-dimensional solitary Rossby waves. *Oceanology,* **23,** 545–552.

Legras, B., P. Santangelo, and R. Benzi, 1988: High resolution numerical experiments for forced two-dimensional turbulence. *Europhys. Lett.,* **5,** 37–42.

Melander, M. V., J. C. McWilliams, and N. J. Zabusky, 1987a: Axisymmetrization and vorticity-gradient intensification of an isolated two-dimensional vortex through filamentation. *J. Fluid Mech.,* **178,** 137–159.

——, N. J. Zabusky, and J. C. McWilliams, 1987b: Asymmetric vortex merger in two dimensions: Which vortex is ''victorious''? *Phys. Fluids,* **30,** 2610–2612.

Montgomery, M. T., and L. J. Shapiro, 1995: Generalized Charney–Stern and Fjørtoft theorems for rapidly rotating vortices. *J. Atmos. Sci.,* **52,** 1829–1833.

——, and R. J. Kallenbach, 1997: A theory for vortex Rossby-waves and its application to spiral bands and intensity changes in hurricanes. *Quart. J. Roy. Meteor. Soc.,* **123,** 435–465.

——, and J. Enagonio, 1998: Tropical cyclogenesis via convectively forced vortex Rossby waves in a three-dimensional quasigeostrophic model. *J. Atmos. Sci.,* **55,** 3176–3207.

Orlandi, P., and G. J. F. van Heijst, 1992: Numerical simulations of tripolar vortices in 2d flow. *Fluid Dyn. Res.,* **9,** 179–206.

Polvani, L. M., and X. J. Carton, 1990: The tripole: A new coherent vortex structure of incompressible two-dimensional flows. *Geophys. Astrophys. Fluid Dyn.,* **51,** 87–102.

Reasor, P. D., M. T. Montgomery, F. D. Marks, and J. F. Gamache, 2000: Low-wavenumber structure and evolution of the hurricane inner core observed by airborne dual-Doppler radar. *Mon. Wea. Rev.,* **128,** 1653–1680.

Rossi, L. F., J. F. Lingevitch, and A. J. Bernoff, 1997: Quasi-steady monopole and tripole attractors for relaxing vortices. *Phys. Fluids,* **9,** 2329–2338.

Samsury, C. E., and E. J. Zipser, 1995: Secondary wind maxima in hurricanes: Airflow and relationship to rainbands. *Mon. Wea. Rev.,* **123,** 3502–3517.

Schubert, W. H., M. T. Montgomery, R. K. Taft, T. A. Guinn, S. R. Fulton, J. P. Kossin, and J. P. Edwards, 1999: Polygonal eyewalls, asymmetric eye contraction, and potential vorticity mixing in hurricanes. *J. Atmos. Sci.,* **56,** 1197–1223.

Shapiro, L. J., and H. E. Willoughby, 1982: The response of balanced hurricanes to local sources of heat and momentum. *J. Atmos. Sci.,* **39,** 378–394.

Smith, G. B., and M. T. Montgomery, 1995: Vortex axisymmetrization: Dependence on azimuthal wavenumber or asymmetric radial structure changes. *Quart. J. Roy. Meteor. Soc.,* **121,** 1615–1650.

Sutyrin, G. G., 1989: Azimuthal waves and symmetrization of an intense vortex. *Sov. Phys. Dokl.,* **34,** 104–106.

van Heijst, G. J. F., R. C. Kloosterziel, and C. W. M. Williams, 1991: Laboratory experiments on the tripolar vortex in a rotating fluid. *J. Fluid Mech.,* **225,** 301–331.

Willoughby, H. E., 1990: Temporal changes of the primary circulation in tropical cyclones. *J. Atmos. Sci.,* **47,** 242–264.

——, J. A. Clos, and M. G. Shoreibah, 1982: Concentric eyewalls, secondary wind maxima, and the evolution of the hurricane vortex. *J. Atmos. Sci.,* **39,** 395–411.

——, J. M. Masters, and C. W. Landsea, 1989: A record minimum sea level pressure observed in Hurricane Gilbert. *Mon. Wea. Rev.,* **117,** 2824–2828.